

General Disclaimer

One or more of the Following Statements may affect this Document

- This document has been reproduced from the best copy furnished by the organizational source. It is being released in the interest of making available as much information as possible.
- This document may contain data, which exceeds the sheet parameters. It was furnished in this condition by the organizational source and is the best copy available.
- This document may contain tone-on-tone or color graphs, charts and/or pictures, which have been reproduced in black and white.
- This document is paginated as submitted by the original source.
- Portions of this document are not fully legible due to the historical nature of some of the material. However, it is the best reproduction available from the original submission.

"Made available under NASA sponsorship
in the interest of early and wide dis-
semination of Earth Resources Survey
Program information and without liability
for any use made thereof."

597
E83-10088

CR-149598

THE INTERMEDIATE WAVELENGTH MAGNETIC ANOMALY FIELD
OF THE NORTH PACIFIC AND POSSIBLE SOURCE DISTRIBUTIONS

J.L. LaBrecque¹, S.C. Cande¹, and R.D. Jarrard²

¹Lamont-Doherty Geological Observatory
of Columbia University
Palisades, N.Y. 10964

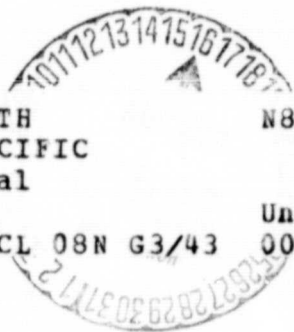
²Arco Oil and Gas Company
Dallas, Texas

(E83-10088) THE INTERMEDIATE WAVELENGTH
MAGNETIC ANOMALY FIELD OF THE NORTH PACIFIC
AND POSSIBLE SOURCE DISTRIBUTIONS Final
Report (Lamont-Doherty Geological
Observatory) 78 p HC A05/MF A01

N83-14596

Unclas

CSCL 08N G3/43 00088



RECEIVED

AUG 5, 1982

SIS/9026

M-018

FINAL REPORT

Final Report for NASA Grant NAS-5-25891

ORIGINAL CONTAINS
COLOR REPRODUCTIONS

ORIGINAL PAGE IS
OF POOR QUALITY

TABLE OF CONTENTS

Title Page.....	i
Table of Contents.....	ii
List of Figures.....	iii
Abstract.....	iv
Introduction.....	1
Data Set.....	4
Technique.....	4
Total Field Secular Variation Anomalies.....	10
Intermediate Wavelength Total Field Anomalies.....	12
Conclusion.....	20
Acknowledgements.....	21
References.....	22
Figure Captions.....	28
Figures.....	34
Appendix.....	64

ORIGINAL PAGE IS
OF POOR QUALITY

LIST OF FIGURES

- Figure 1: Filtered sea-surface field.
Figure 2: MAGSAT anomaly field.
Figure 3: Total secular variation map.
Figure 4: Bathymetric map of the North Pacific.
Figure 5: Track locations.
Figure 6: Distribution of cruises in time.
Figure 7: Application of the Gaussian filter.
Figure 8: Spectral response of the Gaussian filter.
Figure 9: Correlation between DS, DST, and A_p .
Figure 10: Distribution of DST and A_p .
Figure 11: Correlation between observed secular variation and SQ model.
Figure 12: Latitudinal variation of $6^\circ \times 6^\circ$ anomaly field.
Figure 13: Example of regression analysis.
Figure 14: Secular variation anomaly.
Figure 15: $6^\circ \times 6^\circ$ filtered sea surface anomaly.
Figure 16: MAGSAT field in the mid-Pacific.
Figure 17: Sea surface field in the mid-Pacific.
Figure 18: The Emperor anomaly in the MAGSAT field.
Figure 19: The Emperor anomaly in the sea surface field.
Figure 20: North Pacific plate motion.
Figure 21: Magnetic models of seamounts.
Figure 22: C1007 profiles over the mid-Pacific.
Figure 23: Filtered sea surface anomaly over the western Pacific.
Figure 24: MAGSAT field over the western Pacific.
Figure 25a: Crustal thickness versus anomaly amplitude.
Figure 25b: Heat flow versus anomaly amplitude.
Figure 26: Magnetic model for the western Pacific.
Figure 27: C.V. Hudson profiles in the eastern Pacific.
Figure 28: Magnetic model for the eastern Pacific.

ORIGINAL PAGE IS
OF POOR QUALITY

ABSTRACT

Employing a technique that eliminates external field sources and the effects of strike aliasing, we have extracted from marine survey data the intermediate wavelength magnetic anomaly field for $|B|$ in the North Pacific. A strong correlation exists between this field and the MAGSAT field although we can detect a directional sensitivity in the MAGSAT field. The intermediate wavelength field is correlated to tectonic features. Island arcs appear as positive anomalies of induced origin likely due to variations in crustal thickness. Seamount chains and oceanic plateaus also are manifested by strong anomalies. The primary contribution to many of these anomalies appears to be due to a remanent magnetization.

The source parameters for the remainder of these features are presently unidentified ambiguous. This study indicates that the sea surface field is a valuable source of information for secular variation analysis and the resolution of intermediate wavelength source parameters.

THE INTERMEDIATE WAVELENGTH MAGNETIC ANOMALY FIELD
OF THE NORTH PACIFIC AND POSSIBLE SOURCE DISTRIBUTIONS

Introduction

The object of this study is to investigate the feasibility of extracting intermediate wavelength magnetic anomalies of wavelengths between 3000 km and 300 km from total field data acquired in marine magnetic surveys. The long term objectives of the research are to:

- (1) determine the distribution of intermediate wavelength anomalies over the world's oceans,
- (2) determine the extent to which MAGSAT describes the distribution of these anomalies,
- (3) determine the sources of the intermediate wavelength magnetic field.

Examination of the intermediate wavelength magnetic anomaly field of the ocean basins offers the possibility of constraining some of the ambiguities which affect magnetic anomaly analysis over continental areas. For the most part present models for the development of oceanic lithosphere are relatively simple. The age of the oceanic lithosphere is well known and models for the lithospheric structure are simple and supported by an extensive data set. Thermal sources and gradients have been measured and delineated. Furthermore isostatic constraints require a bathymetric expression for bulk changes in lithospheric structure. Therefore, the variables which might determine the magnetic source distribution are relatively well constrained in oceanic lithosphere.

In the following pages we will describe the techniques which were developed to recover the intermediate wavelength total field anomalies over the North Pacific from marine survey data. We feel that the investigation has been extremely successful though much remains to be done in extending the areas of the study to other oceanic basins and tectonic features. Also, the

sources of the observed intermediate wavelength anomalies must be studied in far greater detail than has been possible with the limited resources available in this pilot study. The technique is capable of successfully separating intermediate wavelength total field anomalies and of providing a high resolution record for secular variation during the period 1960 to 1980. Furthermore, the sea surface data set provides a higher resolution than the MAGSAT field, due to the closer proximity of the sea surface data to the lithospheric source bodies and eliminates the directional or longitudinal attenuation which is characteristic of present processing for the polar orbiting MAGSAT data. The results of the North Pacific study show that the anomalies observed in the MAGSAT and POGO fields are also observable in the sea surface data set and that many of these anomalies can be more strongly associated with tectonic features due to the increased resolution of the sea surface field. The two data sets are complementary, in areas of reduced track density the MAGSAT field provides higher resolution and the MAGSAT data set also records the all important vector field data. In areas of high track density the sea surface data can be used to refine the MAGSAT data processing techniques and also provide further constraints on source models.

Harrison and Carle (1981) recently examined the spectral content of several long profiles over the Pacific and Atlantic oceans. They concluded that intermediate wavelength energy was observable in marine magnetics profiles. Shure and Parker (1981) introduced a caveat in such studies of long profiles. Spectral analyses of long profiles assume that all anomalies are lineated perpendicular to the track. The spectral analyses are therefore highly susceptible to three dimensional anomalies or oblique lineations which fold energy into the longer wavelength portions of the spectrum. For convenience, we assign the term 'strike-aliasing' to this phenomenon. Shure and

Parker (1981) concluded their study by bandpass filtering the magnetic anomaly pattern in an area of the Juan de Fuca Ridge. The area was chosen because of its dense magnetic surveys perpendicular to the strike of the seafloor anomaly pattern. Shure and Parker concluded that intermediate wavelength anomalies were not present within their study area. The MAGSAT field and our study (Figure 12) both show that the region of the Juan de Fuca ridge is a region of subdued magnetic anomalies in the intermediate wavelengths which strike perpendicular to the track direction. Therefore, it cannot be concluded from the Shure and Parker study that strike aliasing is the cause of the observed intermediate wavelength field in sea surface profiles.

Our study is designed to circumvent the problem of 'strike-aliasing' by filtering randomly oriented profiles over large areas. Our technique is similar to one adopted by Nomura (1979) in a study of the North Pacific intermediate wavelength field but differs in methods of external field correction, data density and areal coverage.

Figure 1 shows the results of this study, i.e. the intermediate wavelength total field anomalies obtained from filtered marine anomaly profiles over the North Pacific. Figure 2 displays the MAGSAT anomaly field (Langel et al., 1982) observed at 400 km. above the same region as Figure 1. Though there is some difference between the two fields of Figs. 1 and 2 in the long wavelength regional fields, close examination of the two fields reveals a remarkable correlation which will be discussed later. Figure 3 shows the secular variation of the total field obtained from the marine data set for Epoch 1970. The intermediate wavelength anomaly field displays a strong correlation to bathymetric features (Fig. 4) which will help in the isolation of source bodies and the development of improved analysis techniques for MAGSAT and future satellite magnetic surveys.

ORIGINAL PAGE IS
OF POOR QUALITY

The Data Set:

The data set used in preparing the magnetic anomaly maps (Fig. 1 and Fig. 3) were obtained from Lamont-Doherty data files and the National Geophysical and Solar Terrestrial Data Center (NGSDC). No aeromagnetic data were utilized. The data set consists of 370 ships tracks and over 38,000 filtered data points spanning approximately 1,500,000 nautical miles. Figure 5 displays the track density incorporated in this study. In Figure 6 we show a histogram of the data coverage with respect to time. The data coverage spans the years 1960 to 1980 with a mean about 1970. Therefore we will define our intermediate wavelength and secular variation fields to epoch 1970. Figure 6 might also serve as an indication of the variation in funding for marine geophysical exploration during the past two decades.

The Technique:

The marine data measure magnetic fields from several sources of internal and external origin. Among the external sources are magnetic storms and the associated DS and DST variations, Auroral and Equatorial electrojets, and ionospheric SQ currents Nagata and Fukushima (1971). Other sources such as magnetospheric boundary currents or micropulsations are either of low amplitude or too high a frequency to affect our study. Internal sources include the core field and shallow crustal magnetic distributions of structural and sea floor spreading type caused by induced or remanent magnetization. Lithospheric scale magnetization distributions are thought to be the sources of the intermediate field. Our objective in filtering the surface field is the removal of the anomaly fields due to all sources except those of lithospheric scale and intermediate wavelength within the interval 3000 to 300 km.

All marine data are first reduced to anomaly form using a Pre-MAGSAT reference field of degree 13 furnished by Dr. R. Langel -MAGSAT Project Scientist. The model includes secular variation estimates also to degree 13. The field model serves as a nominal regional field which can easily be substituted later in the analysis. All variations in the potential field for wavelengths greater than 3000 km. are therefore removed from the observed data if the PreMAGSAT field model is correct.

The total field anomalies of wavelength less than 300 km were filtered from the profiles using a Gaussian filter. The random filtered data points were then processed within 2x2 and 6x6 degree bins. The random orientation of the tracks and the areal nature of the study should overcome the effects of strike aliasing. A true test of the effectiveness of our technique lies in the coherence of the final data set and its comparison to the MAGSAT anomaly field.

We have applied a Gaussian weighted filter to all anomaly profiles to eliminate aliasing from shorter wavelength crustal anomalies. The filter is adapted from McKenzie et al. (1980) and has a spectral cutoff of 300 km. We have filtered point-by-point values of the magnetic anomaly $M(\bar{a}_j, t_j)$, computed Solar Quiet Variation $SQ(\bar{a}_j, t_j)$, and DST estimates $DST(\bar{a}_j, t_j)$.

where \bar{a}_j = The position vector of data point

t_j = the time of data point

The Filtered Magnetic anomaly becomes:

$$(1) \quad A(\bar{b}_i, t_i) = \sum_j M(\bar{a}_j, t_j) \omega_j / \sum \omega_j$$

where:

$$\bar{b}_i = \frac{\sum_j \bar{a}_j \omega_j}{\sum_j \omega_j}$$

$$\omega_j = \exp\left(-\frac{\chi_j^2}{\sigma^2}\right)$$

$A(\bar{b}_i, t_i)$ = Averaged anomaly value relocated to point b_i

σ = half width of the Gaussian filter

χ_j = is distance to point a_j from the filter centroid.

The spectral response of the Gaussian antialiasing filter is

$$(2) \quad F(s) = \exp\left(-s^2 \sigma^2 / 4\right)$$

where s = scalar wave number.

Figure 7 shows the application of the filter to a given profile. The filter is applied by moving the centroid of the filter at a given increment along the ship's track. All data within a given radius of the centroid is averaged and the resultant value is assigned to the centroid. The filter is incremented at 50 kilometer intervals along track to eliminate aliasing. Note that the filtered value is assigned to a location defined by unit vector \hat{b}_i which is not necessarily coincident with the filter centroid. The Gaussian half width of $\sigma = 100$ km was chosen to give a low pass cutoff of approximately 300 km wavelength. Figure 8 displays the spectral response of the Gaussian filter applied to the magnetic data set. Figure 4 also displays the expected amplitudes and wavelengths of various internal and external sources to be measured by a shipboard magnetometer moving at 10-15 knots. Note that DST, DS, SQ, and the crustal sources are of sufficient amplitude to cause considerable error if these field components are not properly filtered.

The marine magnetic data are scalar total field measurements. The anomaly field is obtained by removing a reference field model determined from a spherical harmonic expansion. The assumption is made that the observed field vector is in the direction of the reference field vector. This can be expressed as:

$$(3) \quad \begin{array}{c} T(x,y) \\ \text{ANO} \end{array} = \begin{array}{c} T(x,y) \\ \text{OBS} \end{array} - \begin{array}{c} T(x,y) \\ \text{REF} \end{array} \\ \cong -\hat{t}_{\text{REF}}(x,y) \cdot \nabla A_{\text{OBS}}(x,y) + \hat{t}_{\text{REF}}(x,y) \cdot \nabla A_{\text{REF}}(x,y)$$

$$(4) \quad \begin{array}{c} T(x,y) \\ \text{ANO} \end{array} \cong -\hat{t}_{\text{REF}}(x,y) \cdot \nabla A_{\text{ANO}}(x,y)$$

$A(x,y)$ = Magnetic scalar potential

$T(x,y)$ = Magnitude of magnetic field vector

$$\hat{t}(x,y) = l(x,y) \hat{i} + m(x,y) \hat{j} + n(x,y) \hat{k}$$

= unit vector in the direction of the magnetic field vector

$$\hat{t}_{\text{OBS}} \cong \hat{t}_{\text{REF}}$$

x, y, z is the coordinate system pointing in the North, East,

and down direction respectively with direction cosines l, m, n .

Subscripts: OBS, REF, ANO refer to the observed, reference and anomaly fields respectively.

Taking the two dimensional Fourier Transform of equation 4 we obtain

$$(5) \quad \begin{array}{c} T(u,v) \\ \text{ANO} \end{array} = (-1) \left[\begin{array}{c} n*s \\ \text{ANO} \end{array} A(u,v) + i \left(\begin{array}{c} l*uA \\ \text{ANO} \end{array} + \begin{array}{c} m*vA \\ \text{ANO} \end{array} \right) \right]$$

$$\text{where } s = (u^2 + v^2)^{1/2}$$

= scalar wave number

* is the convolution operator

Applying the anti-aliasing filter to equation 3 we obtain

$$F(u,v) = \begin{array}{c} T(u,v) \\ \text{ANO} \end{array} e^{-\frac{c^2 s^2}{4}}$$

Note that if the magnetic field vector is not constant over the study area, the spectrum of the total field anomaly will be convolved or smoothed by the spectrum of the total field direction cosines. The effect is to smear the spectral energy to adjacent wavelengths. For small study areas $\leq 10^6 \text{ km}^2$, $\hat{t}(x,y)$ can be thought of as constant and our filtering process is a bandpass for $3000 \gg \lambda \gg 300 \text{ km}$. Components of the field are not subject to this convolution effect. Therefore, some intermediate wavelength anomalies may appear in the total field pattern and not in the component field.

Fig. 9 displays the correlation between DS, DST, and A_p (Sugiura and Chapman, 1960; Mayaud, 1980). It can be seen that during a large magnetic storm, DS and A_p fall off at approximately equal rates after the main phase of the storm. This may be due to the relationship between substorms and magnetospheric convection. The compilations of Fig. 9 suggest that the contributions of DS can be minimized by excluding data acquired when $A_p > 30$. The remaining ring current field, or DST, can be removed using the estimates of Sugiura (1963) available from the NGSDC, when $A_p < 30$, although the problem of annual variation remains unresolved for the moment.

Figure 10 is a histogram of the occurrence of A_p and DST values for our data set. Less than 5% of the utilized data fall in the $A_p > 30$ range. The effect of the auroral electrojet was avoided by restricting the analysis to latitudes less than 50°N . The equatorial electrojet is also observable in the marine data within the region $\pm 5^\circ$ from the magnetic equator (Handschumacher, 1976). We have not restricted our data in time or area to avoid the effect of the equatorial electrojet; therefore care must be taken in interpretations near the magnetic equator. The location of the magnetic equator is shown in as a stippled line in Figures 1,2,3,14, and 15.

The diurnal variation or SQ can provide a significant level of variation in the observed anomaly pattern. We have removed SQ utilizing the model of Malin (1973). Figure 11 (a,b,c,d,e) display the SQ model values and the variation in filtered anomaly data with respect to local time. A total of over 38,000 filtered data points were examined and the number of data points for each band is shown in the figures. The diurnal variation is clearly observed in the data set and on the average the Malin model effectively removes this field. Yearly, seasonal and daily variations in SQ were not considered. In performing the averaging it was noticed that the mean of the anomaly data showed a latitudinal dependence. Figure 12 displays the plot of filtered anomaly means and SQ means with respect to latitude. The variation in the mean anomaly is presumably due to errors in the low order terms of the MAGSAT regional field.

The ship's field at the sensor is usually less than 5-15 nT, Bullard and Mason (1963), and varies with the ship's heading. Since we are using randomly oriented tracks within a given study area we conclude that the effect is subdued in a large data set. A more serious problem is the effect of poor navigation. Inaccurate navigation results in the calculation of an incorrect reference field which may be several tens of gammas in error. Inspection of individual data sets and the culling of problematic data have reduced the effect of poor quality data in our final compilation.

The filtered values are assembled within $2^\circ \times 2^\circ$ and $6^\circ \times 6^\circ$ bins. The sizes of the bins were chosen to optimize stability of the solutions and spatial resolution. The anomaly values within a given bin are considered to be a function of DST, SQ, secular variation and internal intermediate wavelength sources.

The data within a given bin are approximated by the function

$$A(t) = A_{70} + Vt + \text{DST} + \text{SQ}$$

where

A = observed anomaly (intermediate wavelength bandpass)

A₇₀ = anomaly at epoch 1970

V = secular variation anomaly estimated over the 6°x6° grid

t = time in years since 1970

The application of the DST and SQ estimates significantly improves the regression within most bins. Figure 13 displays a bin centered on 23° North, 171° East. Note the improvement in the distribution of filtered anomaly data with respect to the final linear regression for the corrected bin values. Corrections for SQ tend to reduce the dispersion of filtered anomaly values for a given track line: the DST correction generally improves the regression.

Total Field Secular Variation Anomalies:

The secular variation anomalies (V) were computed as described above by linear regression within 6° x 6° bins. A secular variation anomaly is the error in estimate of secular change of the total field after the removal of the Pre-MAGSAT model (n < 13). Significant secular variation anomalies in the total field are seen at wavelengths shorter than 5000 km and amplitudes as large as 60 nT/yr west of Hawaii. (Figure 14). These anomalies show strong spatial correlation to the total field anomaly pattern in Figure 15 which is referenced to the pre-MAGSAT field. For example compare the anomalies centered on 30N, 175E and 30N, 165W in Figures 14, 15 and 10. This can easily be observed by superimposing the two maps.

Aldredge et al. (1963), Harrison and Carle (1981) and Carle and Harrison (1982) have shown that the low order terms in the potential field expansions

may contribute to high order terms in the total field. Therefore, the observed secular variation anomalies may reflect errors in the secular variation estimates of the Pre-MAGSAT model for $n \leq 13$. Because of suspected inaccuracies in the original reference field, we have calculated the total observed filtered field and its associated secular variation by adding the field estimates of the original model field to the $2^\circ \times 2^\circ$ and $6^\circ \times 6^\circ$ grid values for total field and secular variation respectively. The anomaly field of Figure 1 was calculated by removal of DGRF 1970 Field (IAGA, 1981) to order 10. Figure 2 is a plot of the total observed secular variation, note that the 5000 km wavelength features have disappeared. Some localized short wavelength features do remain in the secular variation field. These features are likely artifacts of strong local anomalies and insufficient data coverage.

Core phenomena might also contribute to secular variation for wavelengths shorter than 3000 km. Lowes (1974) notes that the energy in the secular variation appears to fall off less rapidly than the stationary components. This is likely due to the westward drift of the nondipole field components. Therefore, the remaining short wavelength secular variation anomalies may be due to high order core field phenomena. This is interesting in that we may be able to identify some of the intermediate wavelength anomalies as high order core field phenomena.

Finally we must consider that the abrupt truncation of a reference field at a given order will generate an oscillation or ringing (the Gibbs phenomenon - Chapman and Bartels, p. 561, 1940; Bracewell, 1971) in the anomaly field for wavelengths longer than the high pass cut-off in this case $\lambda > 3000$ km or $n > 13$. Since the reference field for both Figures 15 and 2 (PreMAGSAT reference field) and the MAGSAT and Pogo fields were truncated at $N=13$ we would expect similar ringing phenomena. However, the DGRF reference field was truncated at

order and degree 10 therefore the ringing phenomena should differ between these fields. Similarities between the DGRF field and the MAGSAT field should therefore have physical significance since we can eliminate the Gibbs effect as a cause for anomaly correlations. The bandpass for figure 1 after averaging with $2^{\circ} \times 2^{\circ}$ bins and removal of the degree 10 DGRF is 4000 km to 400 km.

Intermediate Wavelength Total Field Anomalies:

In general a strong correlation exists between the MAGSAT anomaly field Figure 2 and the filtered marine data Figure 1 for the North Pacific. Because the two data sets are derived from independent data sets and different reduction techniques were utilized for each field. The correlation therefore suggests that the techniques applied to each data set are appropriate and that the observed anomalies are not an artifact of processing. Positive anomalies are observed in the satellite and surface fields along the Western Pacific Trench system, (35N, 130E), the Indonesian islands (5N, 130E) and the Central Pacific (25N, 170E). The northwestern Pacific is characterized by high amplitude intermediate wavelength anomalies while the northeastern Pacific exhibits a more subdued pattern. The basement relief in the North Pacific is generally greater in the northwestern Pacific than the northeastern Pacific (Figure 4). The basement relief northwestern Pacific is dominated by lineated seamount chains attributed to hot spot trends or fracture zones (Wuksibm 1965; Morgan, 1973).

A first look at the two intermediate wavelength fields shows that the horizontal gradients of the sea surface data are generally steeper than those of the MAGSAT field. This is expected since the MAGSAT field should be equivalent to the upward continued sea surface data provided no errors exist in either data set. The gradients of the sea surface data generally outline tec-

tonic features such as the western Pacific trench system, the mid Pacific Seamounts, the Hess and Shatsky Rises, the margins of the western Pacific Back Arcs Basins, the Hawaiian Emperor Seamount Chain, and to a lesser extent, the Eastern Pacific Fracture Zones such as the Clipperton, the Clarion and the Mendocino.

Broad anomalies ranging from 1000 km to greater wavelengths are also observed in both fields. The most prominent of these we chose to call the Emperor Anomaly. The Emperor Anomaly at 14 nT., is the largest amplitude anomaly observed in the MAGSAT field over the ocean basins. Our filtered sea surface data set also show this anomaly with a maximum amplitude of 150 nT. focused at the bend of the Emperor Hawaiian seamount chain (Figures 1,2, and 16 to 19) where it intersects the Hess Rise.

The Line Island Chain and Mid-Pacific seamounts separate the broad positive regional anomaly (the Emperor Anomaly) to the north from a generally negative residual field to the south (Figure 1). The anomaly field to the east of the Pacific trench system is generally negative as are the Miocene back arc basins from the Sea of Japan to the Parece Vela Basin. The older Eocene age Philippine Basin displays a relative positive anomaly field (Figures 1, 2 and 23).

The magnetic pattern over the Emperor anomaly of the Western Pacific is observed in both the sea surface data and the satellite field. Figures 16 and 17 display the pattern of the intermediate anomalies with respect to regional bathymetry. The Emperor is bounded on its southern and western margins by a steep negative gradient of 20-40 nT/100km. The southern boundary is strongly correlated to the Mid Pacific Seamount, the Western Boundary also has a seamount lineament and the Shatsky Rise to the Northwest. The Northeastern Boundary is likely the Hess Rise though the maximum of the Emperor Anomaly is

located above the bend in the Emperor Seamount Chain, and the intersection of the Mendocino Fracture Zone.

Though the sharper gradients appear to be due to morphologic features, the broad positive magnetic anomaly of the Emperor Anomaly appears to be related to a zone of high amplitude seafloor spreading type anomalies of Mesozoic age. In Figures 18 and 19 we show the MAGSAT and filtered seasurface fields in relation to the seafloor spreading anomalies. Note that the maximum in the intermediate fields appears to correlate strongly with the maximum amplitude of the seafloor spreading anomalies. The amplitude of the seafloor spreading anomalies may reflect an enhancement in the magnetic mineralogy of the lithospheric plate. This suggests to us that in addition to the magnetic fields of the seamount chains, the Hess and the Shatsky Rises, the region of the Emperor Anomaly may also be associated with a lithosphere of generally higher susceptibility.

Overlaying the magnetic anomaly maps 1 and 2 over the basin bathymetric shows that linear negative anomalies (40-50 nT negative) are located above the older seamounts of the region (Figures 16 and 17). The seamounts of the Mid Pacific are generally Mid to Late Cretaceous in age and were formed during the Cretaceous normal period south of the magnetic equator (Thiede et al., 1981; Lancelot, 1978; Lancelot and Larson, 1975). The Emperor-Hawaiian chain are Late Cretaceous to Cenozoic in age and were formed near 20°N (Kono, 1980, Harrison et al., 1975). The northward motion of the Pacific has moved them to their present location (Fig. 20).

Figures 16 and 17 show that the aggregate magnetic anomaly pattern of these seamounts is strongly negative at sealevel and weakly negative at the satellite altitudes. A comparison of Figures 16 and 17 shows the strong correlation between the MAGSAT and sea surface fields. The figures also show

that decreased sensitivity of MAGSAT to north-south striking anomalies due to its orbital inclination. Note that the Emperor Seamount anomaly is not observed in MAGSAT while the Emperor Trough anomaly is apparent in both fields.

Figures 16 and 17 show that a positive anomaly exists of the Northwest and Northeast corners of the Emperor anomaly. These appear to be associated with zones of thickened crust named the Shatsky and Hess Rises.

Because most large seafloor features $\lambda > 100$ km are isostatically compensated, we expect that intermediate wavelength topography will be reflected in mantle topography. Wasilewski et al. (1979) have suggested that the Moho forms a lower magnetic boundary within the lithosphere. The work of Wasilewski et al. is based on susceptibility measurements of ultramafics. A direct relationship should therefore exist between seafloor topography and intermediate wavelength anomalies if the hypothesis of Wasilewski et al. (1979) is correct and if oceanic relief is isostatically compensated by lithospheric flexure and crustal thickening (Watts, 1978).

The question of whether the observed fields are due to induced or remanent magnetization is especially interesting since an induced anomaly of the amplitude observed over the Mid Pacific Seamounts would require a substantial root and would support Wasilewski's hypothesis. On the other hand a remanent magnetic source could significantly aid in determining absolute plate rotations from paleomagnetic data. In the region covered by Figures 16,17 we have a good record of plate motion and paleomagnetism as recovered by the Deep Sea Drilling Program and the work of such authors as Harrison et al., 1975; Kono, 1980; Lancelot and Larson, 1975; Lancelot, 1978; Thiede et al., 1981; and Vallier et al., 1981. In order to determine the most important component of magnetization we have formulated two simple models. The first model is a 2-dimensional prism of thickness 4 km and magnetization 3.3 A/m (.0033 emu/cc)

and polarity according to references previously mentioned and listed in the figure caption of Figure 21. The second model is an inductively magnetized prism of thickness 13 km and susceptibility 4×10^{-2} SI (.0033 emu/cc). The upper surface of each prism is at 2 km depth. Figure 21 displays the observed anomaly at seafloor and at MAGSAT altitudes. A comparison of the model profiles to the various seamount chains and rises of figures 16 and 17 shows that only for the Marshall-Gilbert, Mid-Pacific and Emperor Seamounts is it possible to distinguish between the two models. The induced anomaly model for the Marshall-Gilbert and Mid Pacific seamounts is much more highly skewed than the observed data. The observed data match the remanent model quite well with the minimum of the anomaly directly over the center of mass. The Emperor Seamounts strongly support a remanent model since the induced model requires a positive anomaly where a negative (-10γ) anomaly is observed in the filtered seafloor field. Unfortunately the North-South lineated anomaly is only slightly recorded in the MAGSAT field. This is presumably due to the directional sensitivity of the MAGSAT field.

Figure 23 displays the filtered sea surface field with respect to the tectonic features of the Western Pacific island arc system. Contours are extended over islands and onto land areas. This is a result of our numerical processing and represents an interpolation or extrapolation of the marine data set. Therefore care must be exercised in interpreting these results. The correlations between the filtered sea surface data and the tectonic structure of the region are surprisingly strong. The similarity of the filtered sea surface field to the MAGSAT field, Figure 24, is generally poor. Some similarity exists along the Japan trench and over the island arcs but the correlation worsens over the back arc system. This may be due to the insensitivity

of the MAGSAT field to north-south lineations which pre-dominate in the region.

One can see a strong correlation in Figure 23 to virtually all known tectonic lineaments. These correlations include local positive anomalies bordering all trenches including the Kuril, Japan, Bonin, Ryukyu, and the Philippine trenches. The only exception being the Mariana trench. A local negative follows the abandoned spreading axis of the Japan Basin, Shikoku and Parece Vela Basins. These basins are likely Miocene to Oligocene in age (Mrozowski and Hayes, 1979; Karig, 1971, 1975; Weissel, 1981; Karig et al., 1975). The older (Eocene) West Philippine Basin (Mrozowski et al., 1982) shows a local positive anomaly. A weak magnetic gradient is observed over the Central Basin Fault and stronger gradients are located along the boundaries of the Philippine Basin.

Though it is quite obvious that the intermediate wavelength anomalies appear to separate regions of the Western Pacific with differing tectonic histories the causes of the magnetic contrast are not obvious and the application of a single model is fraught with contradictions.

The general correlation of moderate heat flow to the Japan-Parece Vela Basin negative anomaly (Yanagisawa et al., 1982) is contradicted by the older (Eocene) and lower heat flow of the Oki-Daito region. Furthermore, maximum heat flow is observed near the island arc system and not near the axis of the negative magnetic anomaly in the Parece Vela Basin (Anderson et al., 1978). Figure 25a displays a plot of heat flow values with respect to magnetic anomaly. Heat flow values were taken from Anderson et al., 1978. Error bars on the heat flow values are 1 standard deviation. Of course the heat flow values may not accurately reflect the true temperature of the lithosphere due to com-

plications such as local hydrothermal circulation or topographic effects. The correlation is nonetheless weak.

Variations in the chemistry of the oceanic lithosphere may reflect changes in the bulk magnetic mineralogy of the basins. However, Deep Sea Drilling results show that the composition of West Philippine, Shikoku, and Parece-Vela Basin basalts closely resemble the mid-ocean ridge basalts with only a slight increase in alkalinity from the Philippine to the Parece Vela basin (Zakariadze, et al., 1980; Dick, et al., 1980; Marsh, et al., 1980; and Wood et al., 1980). For the moment however, the data are too sparse and the correlation are too subtle to draw any conclusions about the relationship between the magnetic anomaly pattern and the chemical composition of the oceanic lithosphere.

There appears to be moderate correlation between crustal thicknesses and magnetic anomaly amplitude along the West Mariana Ridge and within the Parece-Vela Basin and Japan Sea (Fig. 25b). This would support the alternate hypothesis of Yanagisawa, et al., 1982. No similar correlation is observed within the West Philippine Basin though the seismic data are sparse and very few refraction profiles have measured the depth to Moho along the margin of the West Philippine Basin. We note that ultra basic have been dredged from within the Parece Vela Basin which further suggests a thin crust and shallow Moho (Mrozowski and Hayes, 1979).

There is a strong suggestion that intermediate wavelength anomalies delineate tectonic boundaries. The anomalies are moderately correlated to crustal thickness, and weakly correlated to the measured heat flow though problems in obtaining proper measurement environments may have biased the measured heat flow toward lower values and confused the correlation.

In figure 26 we show that a satisfactory model for the western Pacific can be formulated by varying the lower boundary of the magnetic body in accordance with Moho depth as derived from seismic data (Hayes et al., 1978). Thermal conditions within the plate may further alter this crustal thickness model.

Lineated negative anomalies associated with the Mid Pacific seamounts are observed intersecting the Western Pacific trench system (Figures 1 and 23). It is curious that this lineation of the negative anomalies appears to continue into the back-arc region. It is interesting to speculate that the subduction of the Seamount chain may have left a chemical and structural imprint in the developing back-arc as suggested by Kellerher and McCann (1976).

In the eastern Pacific there is a remarkable correlation between the major fracture zones and the intermediate wavelength anomalies observed in the MAGSAT field (Figure 2) and, to a lesser extent, in the $2^{\circ} \times 2^{\circ}$ sea surface field (Figure 1). Since there are relatively few tracks in the eastern Pacific to constrain the sea surface field, the MAGSAT field may be more accurate in depicting this correlation, particularly for east-west lineated anomalies. In Figure 27 we show the geophysical data collected by the C.V. Hudson along a track that ran up longitude $150^{\circ}W$, crossing the Clarion, Molokai, Murray and Mendocino fracture zones. (This is the same profile studied by Harrison and Carle, 1981.) Large magnetic anomalies are observed in the observed and smoothed profiles above the fracture zones. More importantly, it is apparent that the fracture zones correspond to changes in the gradients of the $2^{\circ} \times 2^{\circ}$ sea surface field and in the MAGSAT field as shown in the profiles in the upper part of Figure 27.

We have modeled these anomalies as due simply to a small, .038 SI (.003 emu/cc), susceptibility contrast across the fracture zones (Figure 28). (The

anomalies could also be attributed to a small contrast in the remanent magnetization across the fracture zones.) The fact that the susceptibility (or remanent magnetization) contrasts are maintained over long distances suggests that they may represent long period (30-50 m.y.) variations in the magnetic properties of the crust across the fracture zones. Long term variations in basalt chemistry across fracture zones has been observed in rock samples collected by Challenger drilling in the Atlantic Ocean (Scientific Staff, 1982). The origin of these long term variations are unknown, but may reflect the blocking effect of transform faults on longitudinal flow along the mid-ocean ridge system or as a manifestation of longitudinal cellular convection (Richter and Parsons, 1975).

Conclusion:

We have shown that in regions of relatively high track density, it is possible to recover the intermediate wavelength magnetic anomaly field from marine surveys. Except in cases of north-south lineated anomalies the sea surface anomaly field strongly correlates to the MAGSAT intermediate wavelength field over marine regions therefore verifying the validity of both fields.

In comparing the marine data to the MAGSAT anomaly pattern, the severity of the directional sensitivity has become apparent. Though we cannot quantify this directionality with great precision, a comparison of the Emperor seamount anomaly in the sea surface and the MAGSAT fields suggests that the attenuation of north-south anomalies is approximately a factor of 4. A more careful spectral analysis of the two fields will be required to more accurately quantify this effect.

The observed anomalies over the central correlate strongly with tectonic lineaments of the seafloor. We are able to show that the mid Pacific seamount province and rises are observable in the satellite field and that at least some of these observed anomalies are due to remanent magnetization.

The western Pacific show a strong correlation between tectonic features of the island arc systems and observed positive anomalies. This correlation appears to be due more to variations in crustal thickness than heat flow. The Pacific plate shows many intermediate wavelength magnetic lineaments which may be related to the tectonic history of the Pacific plate. A careful analysis of both the sea surface, and MAGSAT magnetic fields in conjunction with the region's geologic data will undoubtedly reveal more about the sources of these magnetic anomalies and geologic development of the Pacific and other oceanic plates.

Acknowledgements

We wish to acknowledge NASA contract NAS-5-25891 for support of this pilot program and we especially thank Dr. Robert Langel and Harold Oseroff for their patience and support at critical times. Discussions with Drs. Chris Harrison, Bob Parker, Jack Hermance, M. Sugiura, Ron Estes, Mike Mayhew, Gary Karner, Bill Haxby, and Julian Thorne have been especially helpful.

References

- Allredge, L.R., G.D. Van Voorhis, and T.M. Davis, 1963, A magnetic profile around the world, *J. Geophys. Res.*, 68, 3679-3692.
- Anderson, R.N., Langseth, M.G., Hayes, D.E., Watanabe, T., Yasui, M., 1978, Heat Flow Thermal Conductivity, Thermal Gradient, in: *A Geophysical Atlas of the East and Southeast Asian Seas*, ed. Hayes, D.E., SEATAR, pub. Geol. Soc. Am.
- Bracewell, R., 1976, *The Fourier Transform and its Applications*, McGraw Hill Inc., N.Y., 381p.
- Bullard, E.C., and R.G. Mason, *The magnetic field over the ocean; The Sea*, vol. III, M.N. Hill (ed.), Interscience, New York, 1963, 963p.
- Carle, H.M. and Harrison, C.G.A., 1982, A problem in representing the Core Magnetic Field of the Earth Using Spherical Harmonics, *Geophys. Res. Letts.*, v. 9, p. 265-268.
- Chapman, S. and Bartels, J., 1951, *Geomagnetism*, vol. II, Oxford University Press, London, pp. 1049.
- Chase, T.E., Menard, H.W., and Mammerickx, J., 1971, *Topography of the North Pacific*, Institute of Marine Resources, Technical Report Series, (Series TR-17).
- Cochran, J.R., 1973, Gravity and magnetic investigations in the Guiana Basin, Western Equatorial Atlantic, *Geol. Soc. Amer. Bull.*, vol. 84, 3249-3268.
- Dick, H.J.B., Marsh, N.G., Bullen, T.D., 1980, Deep Sea Drilling Project Leg 58 Abyssal Basalts from the Shikoku Basin: Their Petrology and Major-element Geochemistry. in: DeVries Klein, Kobayashi, K., et al., *Initial Reports of the Deep Sea Drilling Project*, v. 58, Washington (U.S. Government Printing Office), p. 843-872.

- Handschumacher, D.W., 1976, Post-Eocene plate tectonics of the eastern Pacific, In: The Geophysics of the Pacific Ocean Basin and Its Margin, G.H. Sutton, M.H. Manghnani, R. Moberly, E.U. McAfee, (eds.), Amer. Geophys. Un. Monogr. 19, 117-202.
- Harrison, C.G.A., Jarrard, R.D., Vacquier, V., and Larson, R.L., 1975, Paleomagnetism of Cretaceous Pacific Seamounts, Geophys. J., v. 42, p. 859-882.
- Harrison, G.G.A., and Carle, H.M., 1981, Intermediate wavelength magnetic anomalies over ocean basins, J. Geophys. Res., in press.
- Hayes, D.E., Houtz, R.E., Jarrard, R.J., Mrozowski, C., Watanabe, T., 1978, Crustal Structure in a Geophysical Atlas of the East and Southeast Asian Seas, ed. Hayes, D.E., SEATAR, Pub. Geol. Soc. of Amer.
- IAGA, Working Group 1, 1981, International Geomagnetic Reference Fields: DGRF 1965, DGRF 1970, DGRF 1975 and IGRF 1980, EOS, v. 62, p. 1169.
- Karig, D.E., 1971, Structural History of the Mariana Island Arc System, Geol. Soc. Am. Bull., 82, p. 323-344.
- Karig, D.E., 1975, Basin Genesis in the Phillipine Sea in: D.E. Karig, J.C. Ingle et al., Initial Reports of the Deep Sea Drilling Project, Vol. XXXL, C.U.S. Government Printing Office, Washington, D.C., p. 857-879.
- Kelleher, J. and McCann, W., 1976, Buoyant Zones, Great Earthquakes, and Unstable Boundaries of Subduction, Jour. Geophys. Res., v. 81, p. 4885-4896.
- Kono, M., 1980, Paleomagnetism of DSDP Leg 55 Basalts and Implications for the Tectonics of the Pacific Plate, in: Jackson, E.D., Koisumi, I., et al., Initial Reports of the Deep Sea Drilling Project, v. 55, Washington (U.S. Government Printing Office), p. 734-752.

- Lancelot, Y., 1978, Relations entre evolution sedimentaire et tectonique de la Plague Pacifique depuis le Cretace Interier, Societe Geologique de France, Memoire, 134.
- Lancelot, Y. and Larson, R.L., 1975, Sedimentary and Tectonic evolution of the northwestern Pacific in: Larson, R.L. and Moberly, R., et al., Initial Reports Deep Sea Drilling Project, 32, Washington (U.S. Government Printing Office, p. 925-939.
- Langel, R.A., Phillips, J.D., and Horner, R.J., 1982, Initial Scalar Magnetic Anomaly Map from MAGSAT, Geophys. Res. Letts., v. 9, p. 269-272.
- Larson, R.L., and Hilde, T.W.C., 1975, A revised time scale of magnetic reversals for the Early Cretaceous and Late Jurassic, J. Geophys. Res., vol. 80, 2586-2594.
- Loves, F.J., 1974, Spatial Power Spectrum of the Main Geomagnetic Field, and Extrapolation to the Core, Geophys. Jour. R. Astro. Soc., 36, 717-730.
- Malin, S.R.C., 1973, Worldwide distribution of geomagnetic tides, Phil. Trans. Roy. Soc. London A., vol. 274, 551-594.
- Marsh, N.G., Saunders, A.D., Tarney, J., Dick, H.J.B., 1980, Geochemistry of Basalts from the Shikoku and Daito Basins, Deep Sea Drilling Project, Leg 58, in: deVries, Klein, Kobayashi, K., et al., Initial Reports of the Deep Sea Drilling Project, v. 58: Washington (U.S. Government Printing Office), p. 805-842.
- Mayaud, P.N., 1980, Derivation meaning, and use of Geomagnetic indices, A.G.U. Monograph 22, pp. 154.
- McKenzie, D., Watts, A., Parson, B., and Roufousse, M., 1980, Planform of mantle convection beneath the Pacific Ocean, Nature, vol. 288, 442-446.
- Morgan, W.J., 1973, Plate motions and deep mantle convection, Geol. Soc. Am. Memoir 132, p. 7-22.

- Mrozowski, C. and Hayes, D.E., 1979, The evolution of the Parece Vela Basin, Eastern Phillipine Sea, EPSL, 46, p. 49-67.
- Mrozowski, C.L., Lewis, S.D., Hayes, D.E., 1982, Complexities in the Tectonic evolution of the West Phillipine Basin, Tectonophysics, v. 82, p. 1-24.
- Nagata, T. and Fukushima, N., 1971, Morphology of Magnetic Disturbance in Encyclopedia of Physics, vol. XLIX/3, Springer-Verlag, S. Flugge and K. Rauer, eds., N.Y., 536p.
- Nomura, M., 1979, Marine geomagnetic anomalies in the western Pacific region, Bull. Earthquake Res., Inst., 11, 1-42, 1979.
- Rabinowitz, P.D. and LaBrecque, J.L., 1979, The Mesozoic South Atlantic Ocean and Evolution of its Continental Margins, J. Geophys. Res., vol. 84, 5973-6002.
- Richter, F.M. and Parsons, B., 1975, On the interaction of two scales of convection in the Mantle, Jour. Geophys. Res., v. 80, p. 2529-2541.
- Scientific Staff, 1982, Elements traced in the Atlantic, Geotimes 27, 21-22.
- Shure, L., and Parker, R.L., 1981, An Alternative explanation for intermediate wavelength magnetic anomalies, Jour. Geophys. Res. (in press).
- Sibouet, J.C., and Mascle, J., 1978, Plate Kinematic implications of Atlantic equatorial fracture zone trends, J. Geophys. Res., vol. 83, 3401-3421.
- Sugiura, M. and S. Chapman, 1960, The Average Morphology of Geomagnetic Storms with sudden Commencements, Abh. Akad. Wiss, Gottingen, Math-Phys. Kl., Sonderheft Nr. 4, 53pp.
- Sugiura, M., 1963, Hourly Values of Equatorial DST for IGY, Goddard Space Flight Center, Greenbelt, Maryland, NASA Rep't X-611-63-131.

- Thiede, J., Dean, W., Rea, D., Vallier, T., Adelseck, C., 1981, The Geologic History of the Mid Pacific Mountains in the Central North Pacific Ocean - A Synthesis of Deep Sea Drilling Studies, in: Thiede, J., Vallier, T.L., et al., Initial Reports of the Deep Sea Drilling Project, 62, Washington, D.C., (U.S. Government Printing Office), p. 1073-1120.
- Vallier, T.L., Rea, D., Walter, D., Thiede, J., Adelseck, C., 1981, The Geology of the Hess Rise, Central North Pacific Ocean, in: Thiede, J., Vallier, T.L., et al., Initial Reports of the Deep Sea Drilling Project, 62, Washington, D.C., (U.S. Government Printing Office), p. 1031-1072.
- Wasilewski, P.J., Thomas, H.H., and Mayhew, M.A., 1979, The MOHO as a Magnetic Boundary, Geophys. Res. Letters, vol. 6, 541-544.
- Watts, A.B., 1978, An Analysis of Isostasy in the World's Oceans; 1. Hawaiian-Emperor Seamount Chain, J. Geophys. Res., 83, 5989-6004.
- Weissel, J.K., 1981, Magnetic lineations in marginal Basins of the Western Pacific, Phil. Trans. R. Soc. Lond., A300, p. 223-247.
- Wilson, J.T., 1965a, Evidence from ocean islands suggesting movement in the Earth, in: Blakett, P.M.S., Bullard, E., and Runcorn, S.K., eds. A symposium on continental Drift, Roy. Soc. London Phil. Trans. Ser. A, vol. 250, p. 145-167.
- Wood, D.A., Joron, J.C., Marsh, N.G., Tarney, J., Treuil, M., 1980, Major- and Trace element variations in Basalts from the North Philippine Sea drilled during Deep Sea Drilling Project Leg 58: A comparative study of Back-Arc-Basin Basalts with Lava series from Japan and mid-ocean ridges. in: deVries, Klein, Kobayashi, K., et al., Initial Reports of the Deep Sea Drilling Project, v. 58: Washington (U.S. Government Printing Office), p. 873.

Yanagisawa, M., Kono, M., Yukutake, T., Fukushima, N., 1982, Preliminary interpretation of Magnetic Anomalies over Japan and its surrounding area, Geophys. Res. Lettrs., v. 9, n. 4, p. 322.

Zakariadze, G.S., Sobolev, A.G., Suschevskaya, N.M., and Dmitriev, L.V., 1980, Petrology of Basalts of Holes 447A, 449, and 450, South Philippine Sea Transect, Deep Sea Drilling Project Leg 59, in: Kroenke, L., Scott, R. et al., Initial Reports of the Deep Sea Drilling Project, Leg 59. Washington (U.S. Government Printing Office), p. 669.

Figure Captions

Figure 1: Filtered seasurface data for the bandpass 4000 km to 400 km as described in the text. The anomaly field is with respect to the DGRF 1970 reference field (IAGA, 1981). The magnetic equator is indicated as a stipled line.

Figure 2: MAGSAT anomaly field from $2^{\circ} \times 2^{\circ}$ averages. Average altitude is 400 km (Lange et al., 1982).

Figure 3: Map of total field secular variation as derived from the filtered sea surface data. The magnetic equator is indicated by a stipled line.

Figure 4: Bathymetric map of the region from Chase et al., with DSDP drill sites indicated.

Figure 5: Track locations of the data set used in this study.

Figure 6: A histogram of the data set distribution in time. Note that the data set is normally distributed in time about 1970.

Figure 7: Application of the Gaussian filter to a measured magnetic anomaly profile.

Figure 8: Spectral Response of the Gaussian antialiasing filter. Marine crustal sources are assumed to be largely due to seafloor spreading type anomalies of short wavelength and high amplitude.

Figure 9: A correlation between the temporal variations in DS, DST and Ap.

Figure 10: Frequency of DST and Ap values in the marine data set.

Figure 11: Correlation between observed diurnal variation and the SQ model (Malin, 1973) utilized in this study. Data are divided into 10° degree latitudinal bands.

Figure 12: Illustration showing the the PreMAGSAT referenced anomaly field of Figure 15 displays a strong latitudinal variation presumably due to field error. The SQ model is stable throughout the region. Diurnal is the mean anomaly value for each latitudinal band of Fig. 11. SQ is the mean model value for each band.

Figure 13: Application of the regression analysis to data within a $2^{\circ} \times 2^{\circ}$ km at 22° N and 170° East. Note that corrections for DST and SQ significantly improve the regression. It was found that better stability in the secular variation estimation could be obtained for 6×6 degree bins.

Figure 14: Secular variation anomaly field estimated from 6×6 degree bins referenced to the Premag I field. Note the oscillation in values about the Hawaii suggesting an error in the model.

Figure 15: $6^{\circ} \times 6^{\circ}$ anomaly field derived from the PreMAGSAT field. Note that the major secular variation anomalies of Figure 14 also appear in the anomaly field, particularly in the region of Hawaii. This indicates the sensitivity of the anomaly field to the selected reference field.

Figure 16: MAGSAT field contoured at a .5nT contour interval. Units are .1nT. Note that there is a slight negative above the Emperor Seamount chain.

Figure 17: Sea surface filtered magnetic anomaly referenced to DGRF 1970 field. Contour interval is 10 nT. Stipled zones are regions above the 4000 meter isobath. Note the strong correlation to the MAGSAT field and Figure 16. Lineated negative anomalies follow the mid-Pacific seamounts, the Marshall-Gilbert and Emperor Sea-

mounts. Positive anomalies overlie the Shatsky and Hess Rises and the Emperor Seamounts.

Figure 18: MAGSAT field referenced to the observed seafloor spreading anomalies (Larson and Hilde, 1975).

Figure 19: Filtered sea surface field with respect to the seafloor spreading anomalies (Larson and Hilde, 1975). Note that the seafloor spreading anomalies of a given age fall off in amplitude as the Emperor anomaly decreases in amplitude. We take this as evidence for a regional variation in crustal lithology emplaced during the creation of this portion of the mid-Pacific in the Jurassic and Early Cretaceous.

Figure 20: Plate motion diagram for DSDP sites as calculated by Lancelot and Larson 1975, and Lancelot (1978).

Figure 21: Model calculations for uniformly magnetized prisms. Two models are considered: (1) Induced prism 200 km wide by 13 km deep. Susceptibility = .04 SI (.0033 emu/cc); (2) Remanent Model = 200 km wide by 4 km deep. Magnetization = 3/3 A/m (.0033 emu/cc). The upper of each model is at 2 km depth. Note that only the remanent and induced models of the Marshall Gilbert/Mid-Pacific and Emperor Seamounts are significantly different.

TABLE

Azimuths, remanent and present field vectors are as follows:

STRUCTURE	AZIMUTH	REMANENT	FIELD	PRESENT	FIELD
		I_R	D_R	I_P	D_P
Emperor Smts	90°	-42°	0°	52°	3°
Hawaiian Smts	30°	31°	0°	40°	7°
Mid-Pacific Smts	0°	-31°	0°	31°	9°
Marshall Gilbert Smts	30°	-31°	0°	31°	9°
Shatsky Rise	315°	-10°	0°	42°	-2°
Hess Rise	355°	-10°	0°	48°	8°

Figure 22: Conrad 1007 profile over the Mid-Pacific seamounts showing upward continued field and MAGSAT anomalies. and the negative anomaly associated with the Mid-Pacific Seamounts.

Figure 23: Filtered sea surface anomaly field over the Western Pacific, 45 nT have been added to the observed anomalies. Note the strong correlation between the region's ridge systems and the magnetic field. A negative follows the abandoned back arc systems of the Japan Basin, Shikoku Basin and the Parece Vela Basin. In general a positive anomaly is observed over the abandoned and present island arc systems. The only exception being the Mariana Arc system.

Figure 24: The MAGSAT field above the Western Pacific. The correlation is much poorer than for the Central Pacific. Presumably this is due

to the directional sensitivity of the MAGSAT field. A linear positive is observed above the Arc trench system but the detail of the sea surface field is not observed.

Figure 25a: Plot of observed heat flow averages versus magnetic anomaly compiled for all stations from Anderson et al., 1970. Heat flow values show a broad scatter which can be reduced somewhat by better station election. However, hydro thermal circulation may have seriously biased the values circulation lower heat flow values.

Figure 25b: Correlation between magnetic anomaly value and the depth to basement as taken from the sonobuoy compilations of two correlations are shown one for the Parece Vela Basin-Shikoku-Japan Basin and the other for the West Phillipine Basin. It should be noted that many variables will affect this correlation including body structure and magnetization distributions. The Parece Vela anomalies are generally linear and North-South trending.

Figure 26: An induced model based on the compilations of the western Pacific seismic data may explain the observed intermediate field in terms of variations in the Moho depth. The susceptibility contrast of the body is .063 SI (.005 emu/cc). The subducting plate has little the effect on the anomaly field. The model appears distorted is horizontal scale due to large vertical exaggeration.

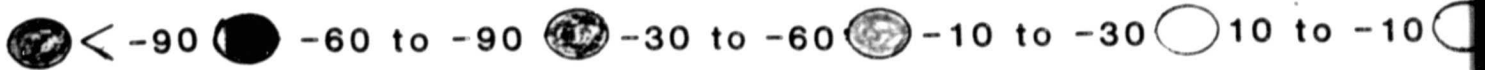
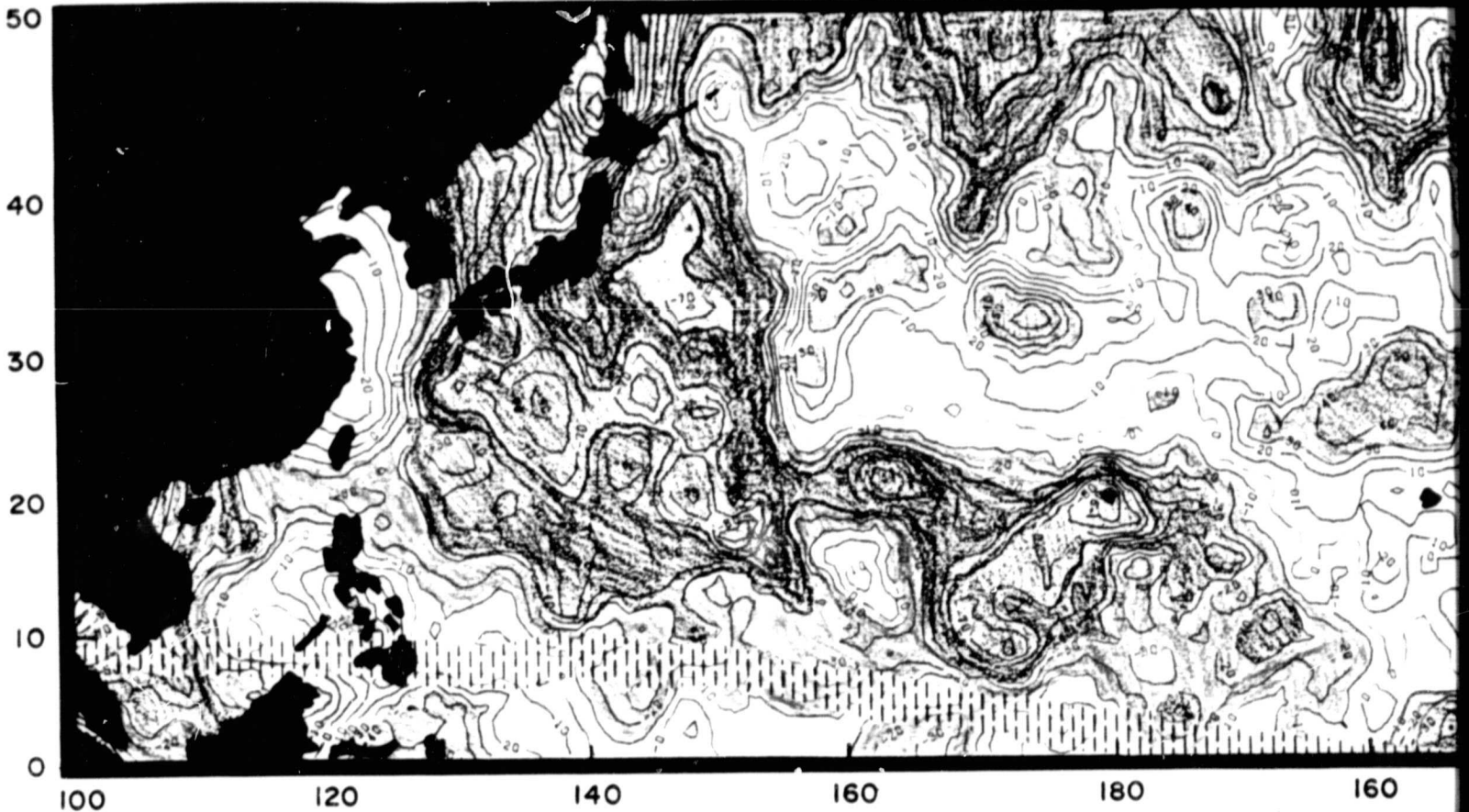
Figure 27: (Lower) Magnetic, gravity and bathymetry from the C.V. Hudson along longitude 150°W. (Upper) Filtered 2°x2° sea surface data, upward continued to 400 km (dashed), and the MAGSAT field along the same track as the Hudson profile.

Figure 28: Model for an induced anomaly due to a susceptibility contrast across the eastern Pacific fracture zones. Stippled bodies have a .038 SI (.003 emu/cc) susceptibility, white bodies have a zero susceptibility, azimuth=0°, $I_p=50^\circ$, $D_p=10^\circ$, field strength=40000 nT. Filtered profile has a bandpass between 400 and 2000 km.

FILTERED SEA SURFACE FIELD

2x2 REGRESSION

100 120 140 160 180 160



UNITS nT.

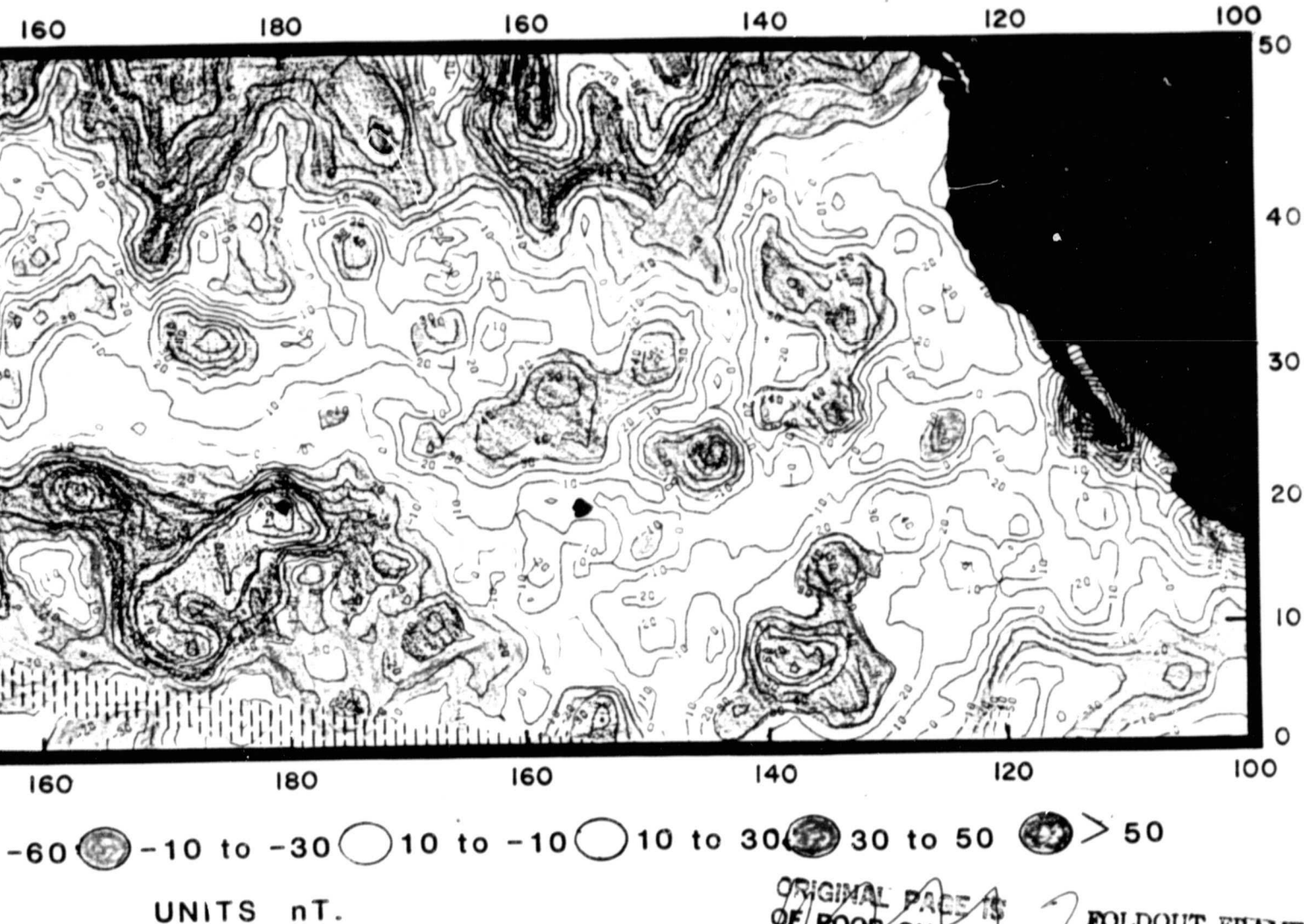
ORIGINAL PAGE
COLOR PHOTOGRAPH

FOLDOUT FRAME

ORIG
COLOR

RED SEA SURFACE FIELD

REFERENCE DGRF 1970



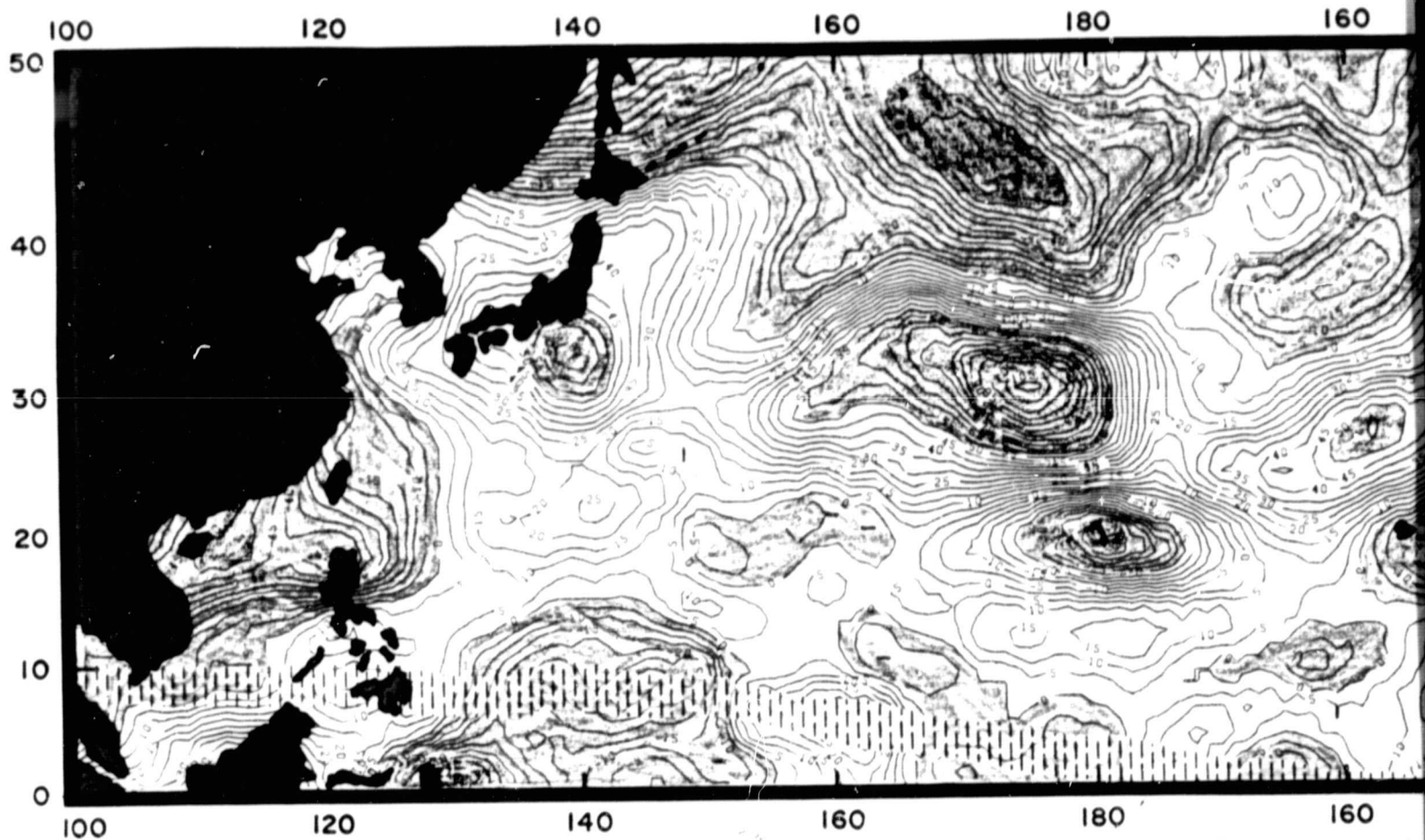
AME

ORIGINAL PAGE
COLOR PHOTOGRAPH

Figure 1

MAGSAT ANOMALY

2x2 AVERAGE



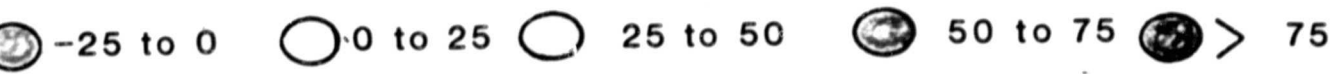
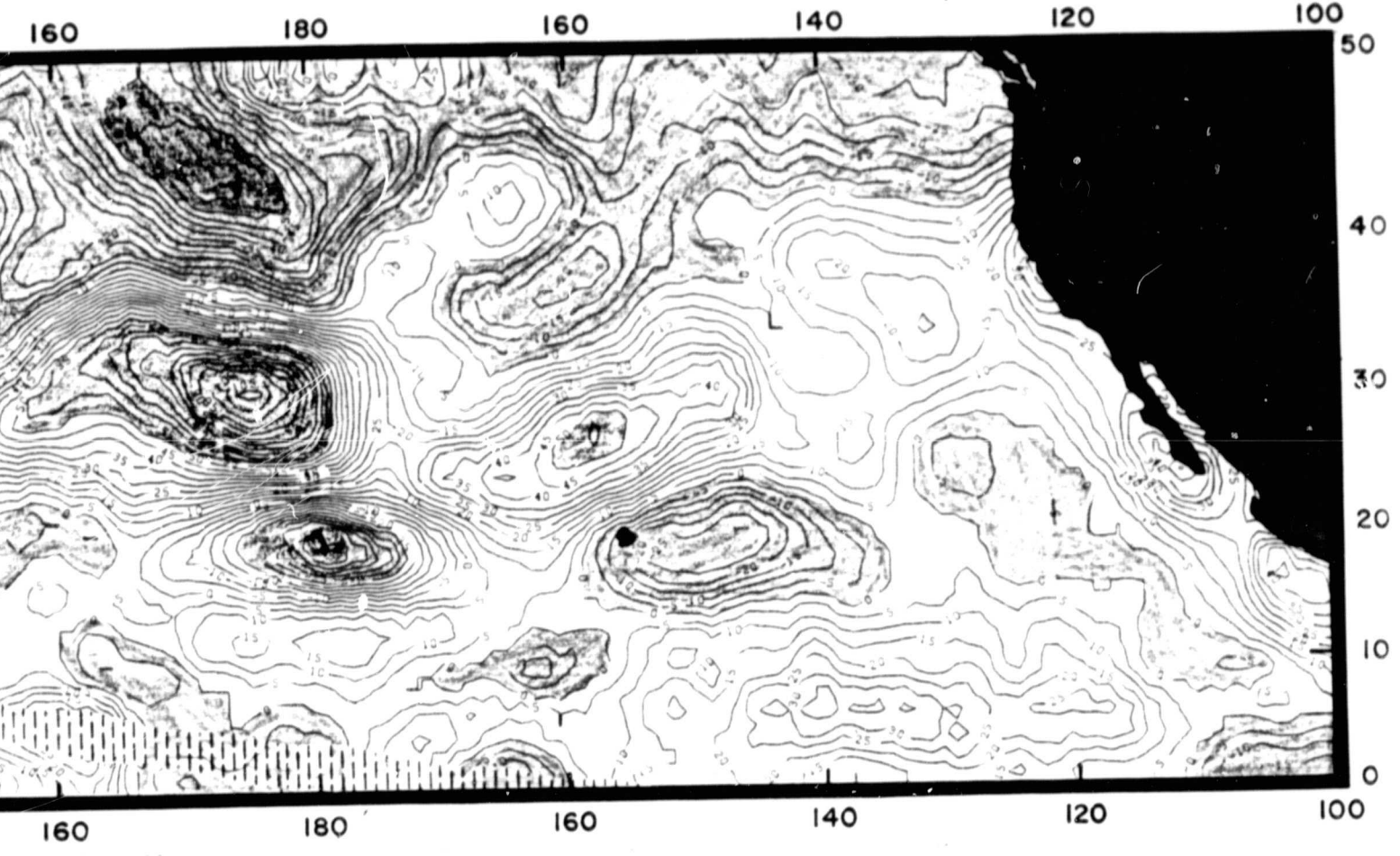
UNITS: .1nT

ORIGINAL PAGE
COLOR PHOTOGRAPH

FOLDOUT FRAME

MAGSAT ANOMALY

EPOCH 1981



UNITS: .1nT

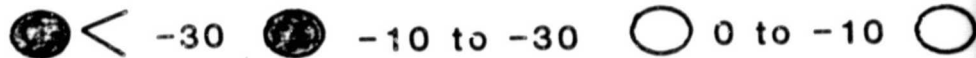
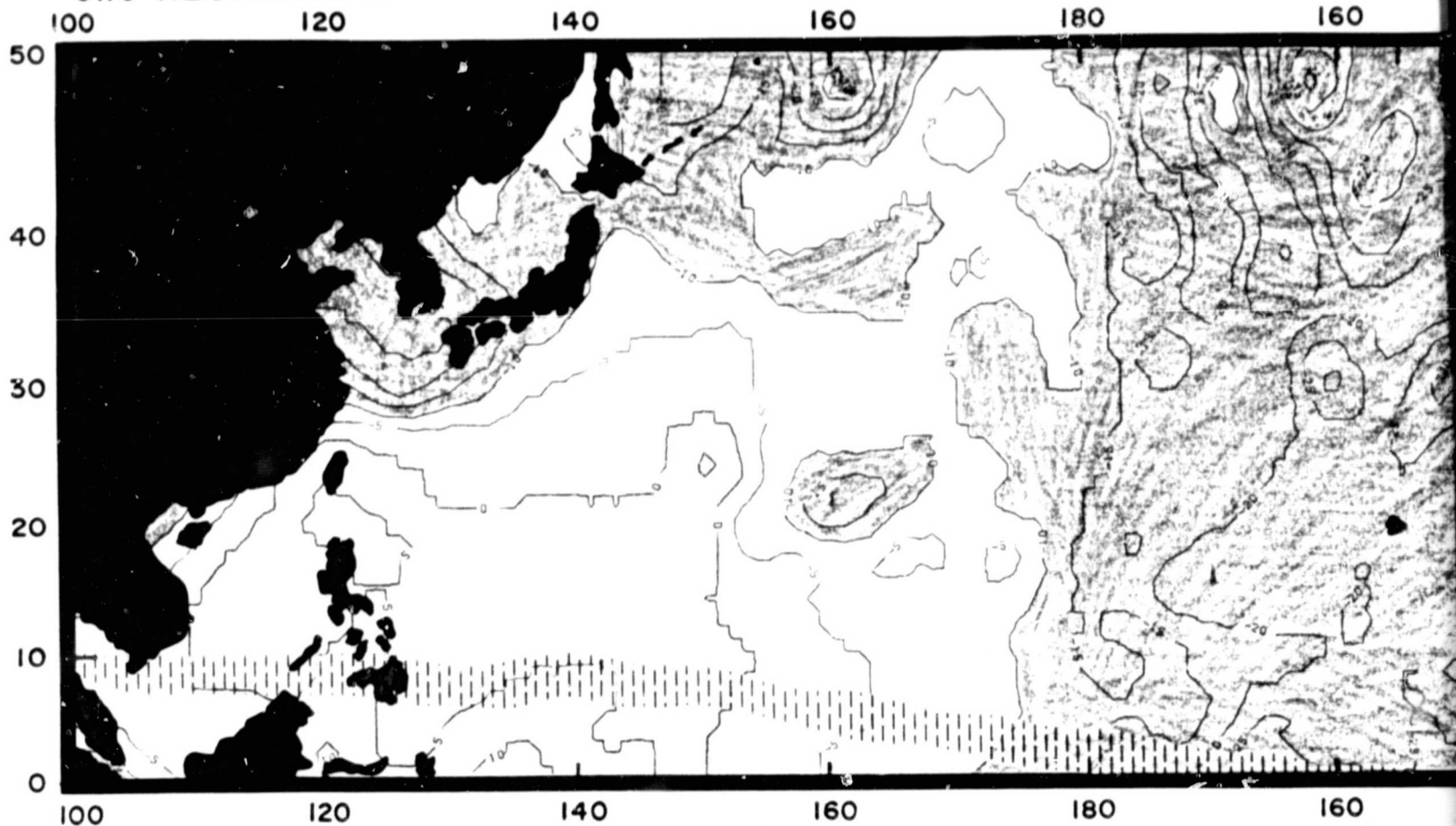
FOLDOUT FRAME

Figure 2

ORIGINAL PAGE
COLOR PHOTOGRAPH

TOTAL SECULAR VARIATION

6x6 REGRESSION



UNITS:nT/yr.

ORIGINAL PAGE
COLOR PHOTOGRAPH

EOLDOUT FRAME

L SECULAR VARIATION

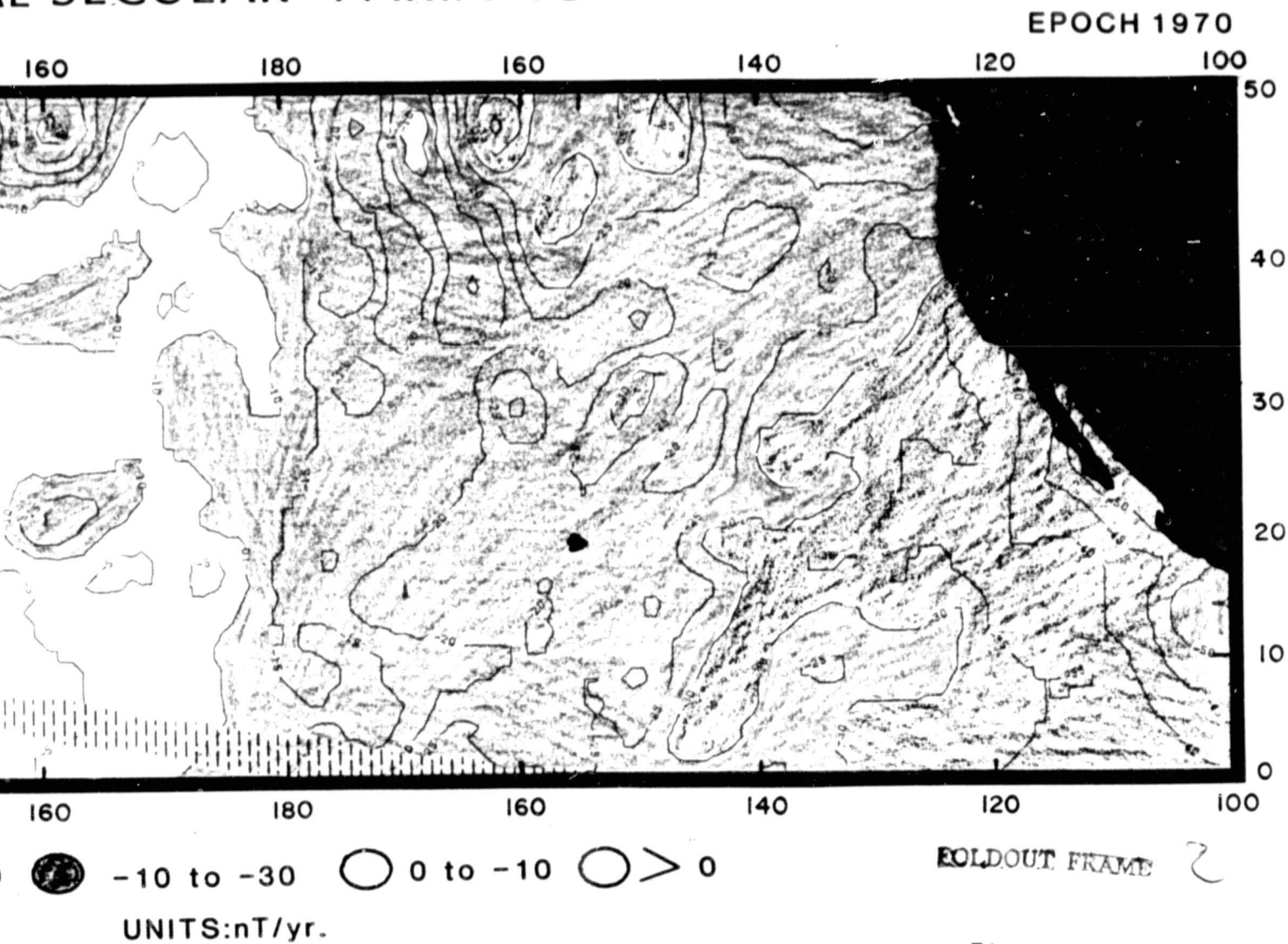
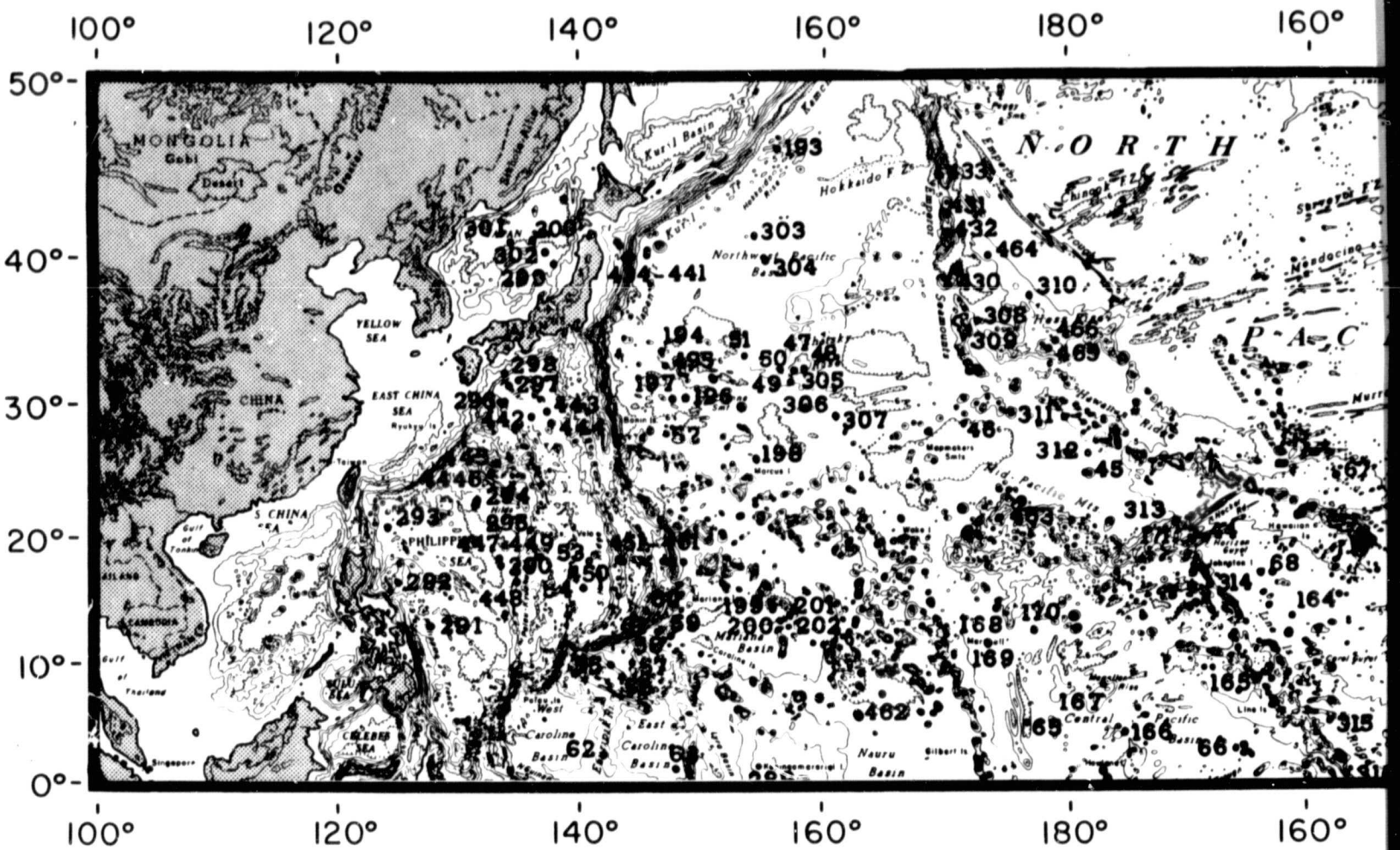


Figure 3

ORIGINAL PAGE
COLOR PHOTOGRAPH

ORIGINAL PAGE IS
OF POOR QUALITY



EOLDOUT FRAME

ORIGINAL PAGE IS
OF POOR QUALITY

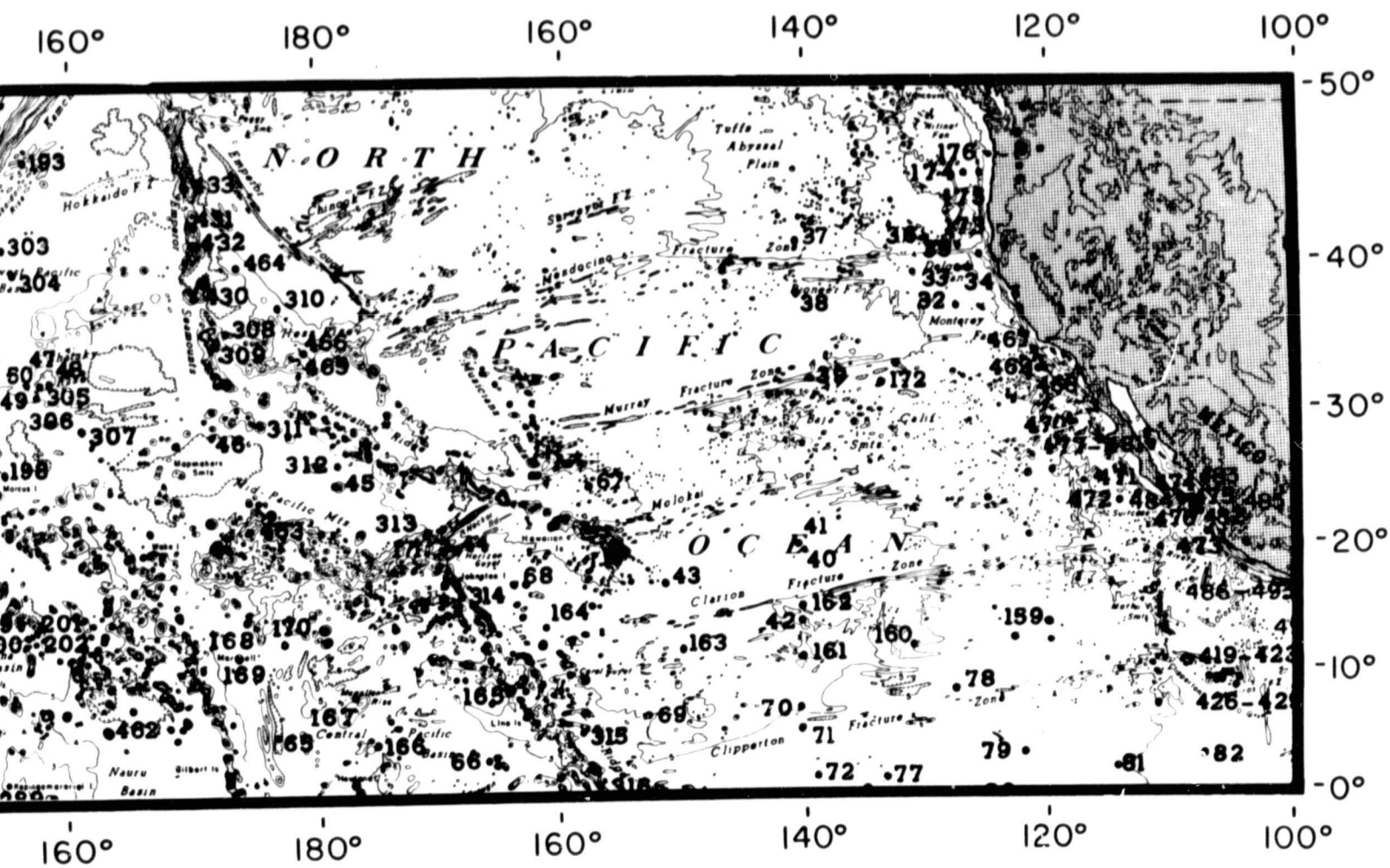


Figure 4

FOLDOUT FRAME

ORIGINAL PAGE IS
OF POOR QUALITY

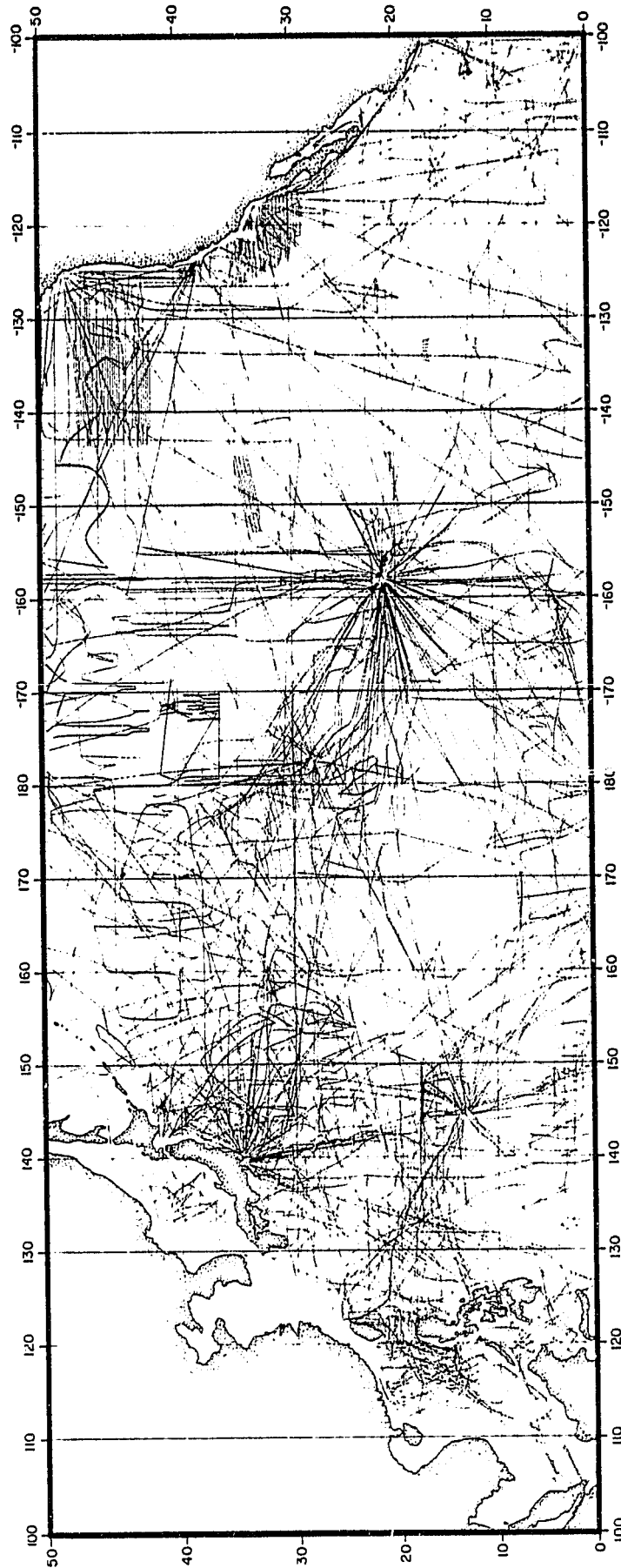


Figure 5

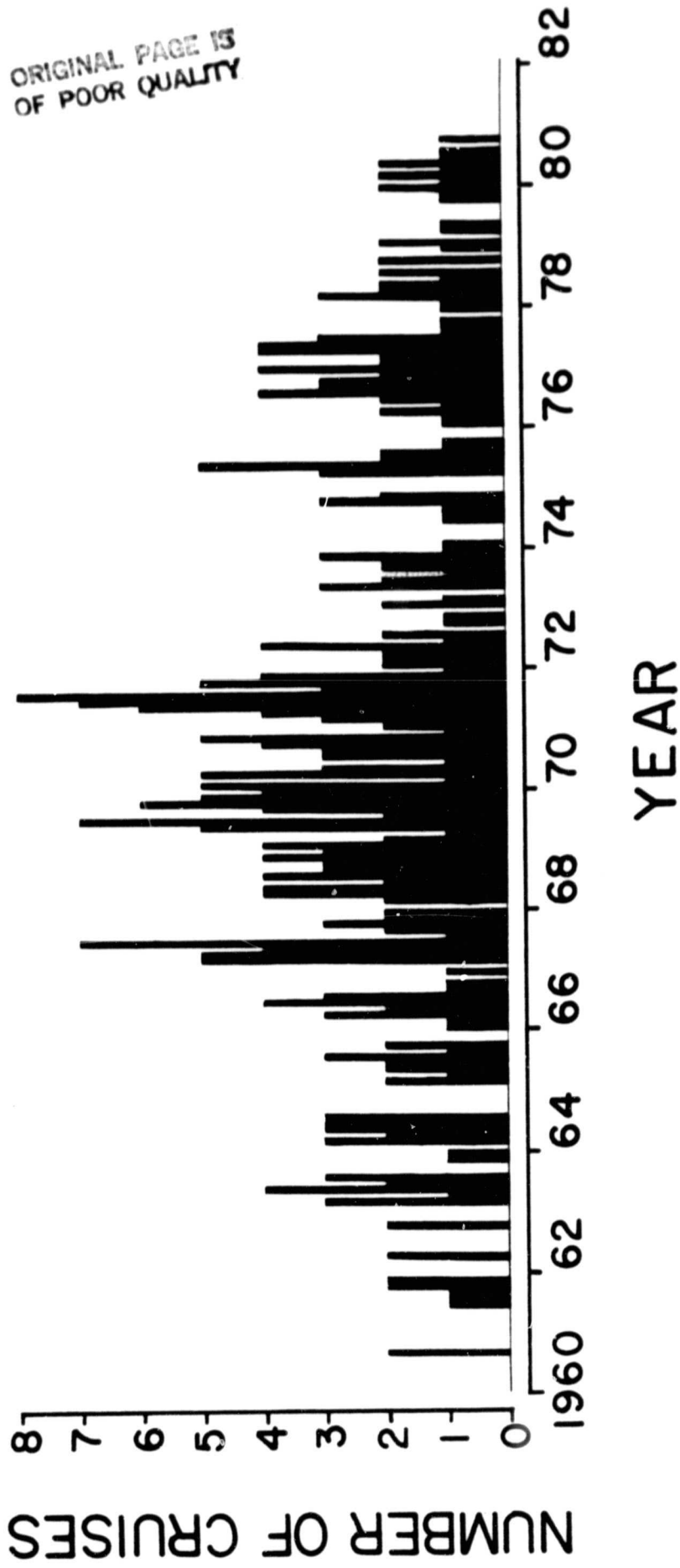


Figure 6

ORIGINAL PAGE IS
OF POOR QUALITY

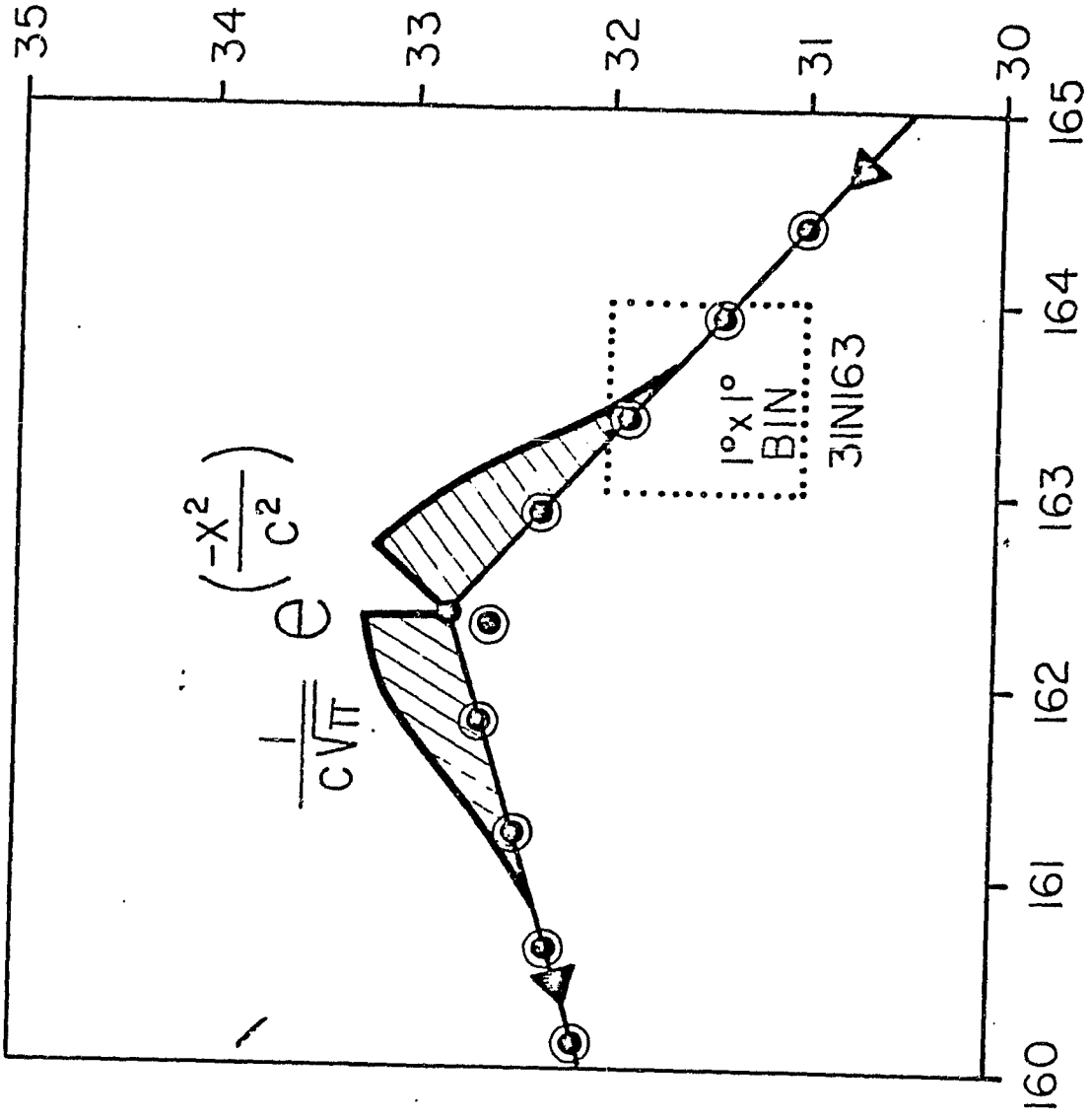


Figure 7

ORIGINAL PAGE IS
OF POOR QUALITY

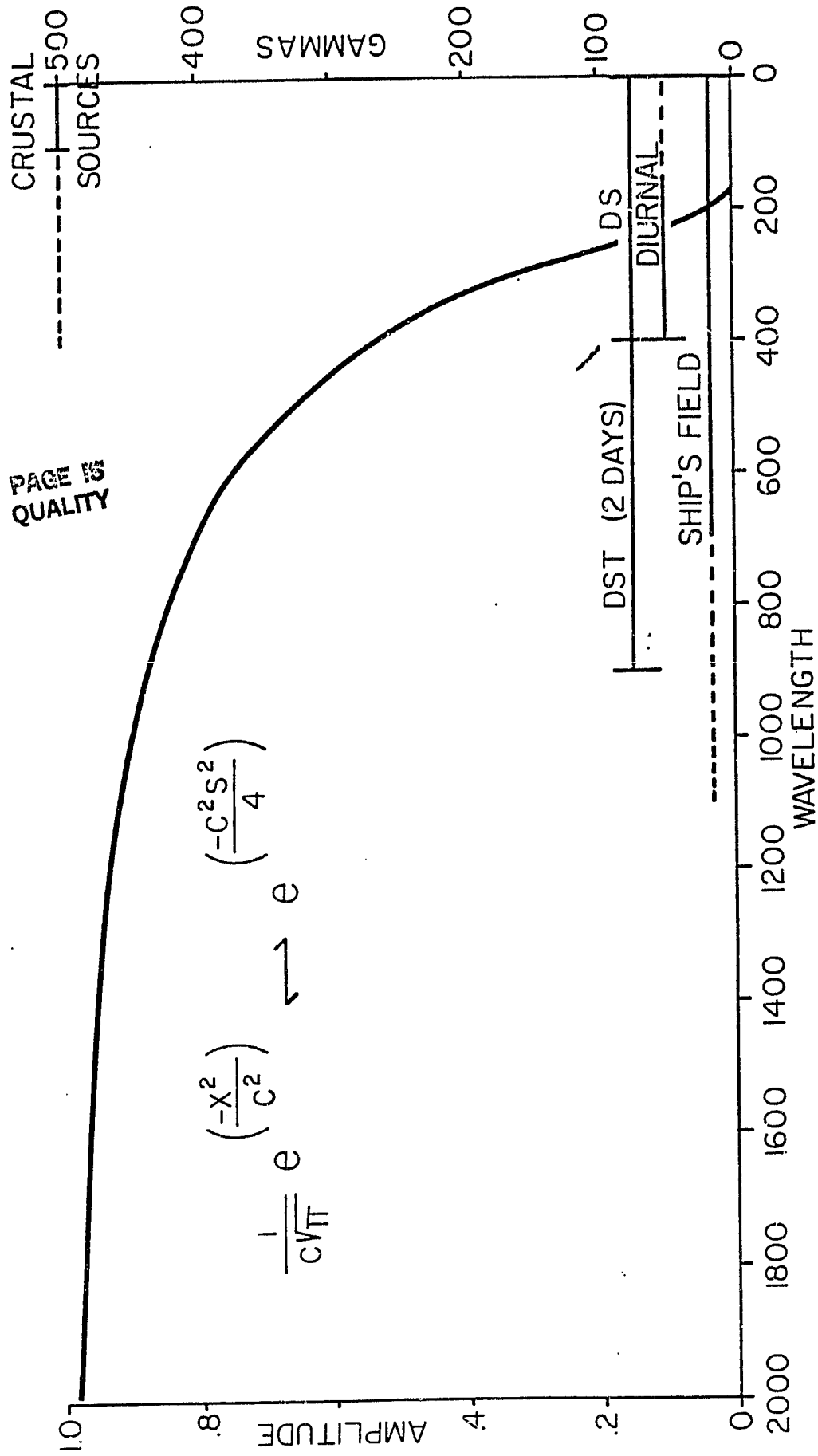
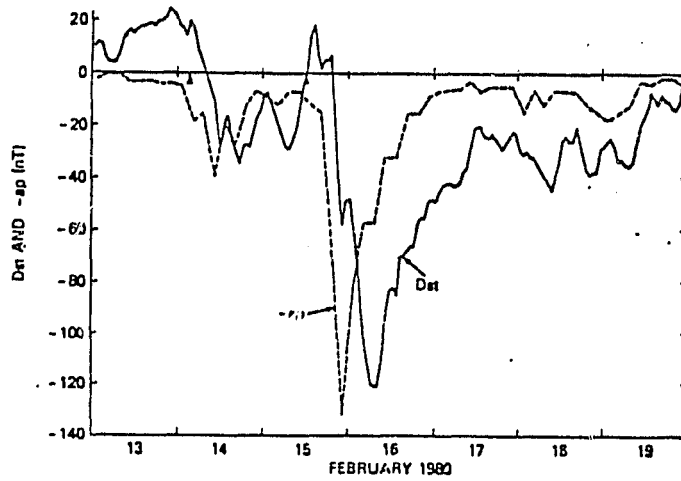
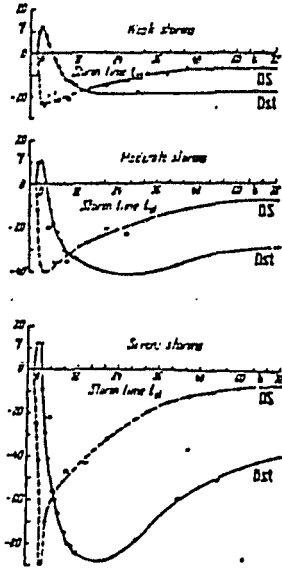


Figure 8

ORIGINAL PAGE IS
OF POOR QUALITY

Figure 9

A comparison of the rates of evolution of $Dst(t)$ and the double amplitude of the first harmonic component of $DS(t)$ at mean geomagnetic latitude 30° . [After Sugino and Chapman, 1960.]



Magnetic indices Kp , ap , and Dst for the magnetic storm of February 15-17, 1979.

ORIGINAL PAGE IS
OF POOR QUALITY.

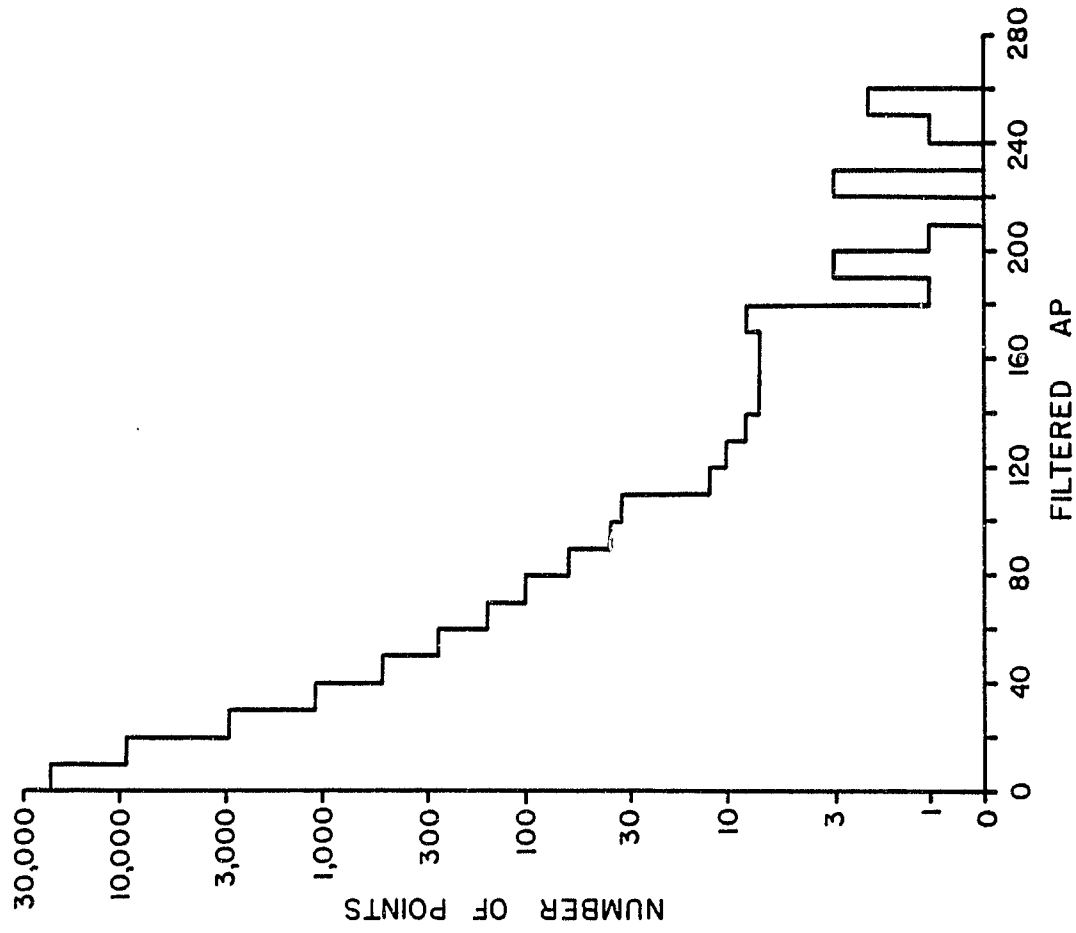
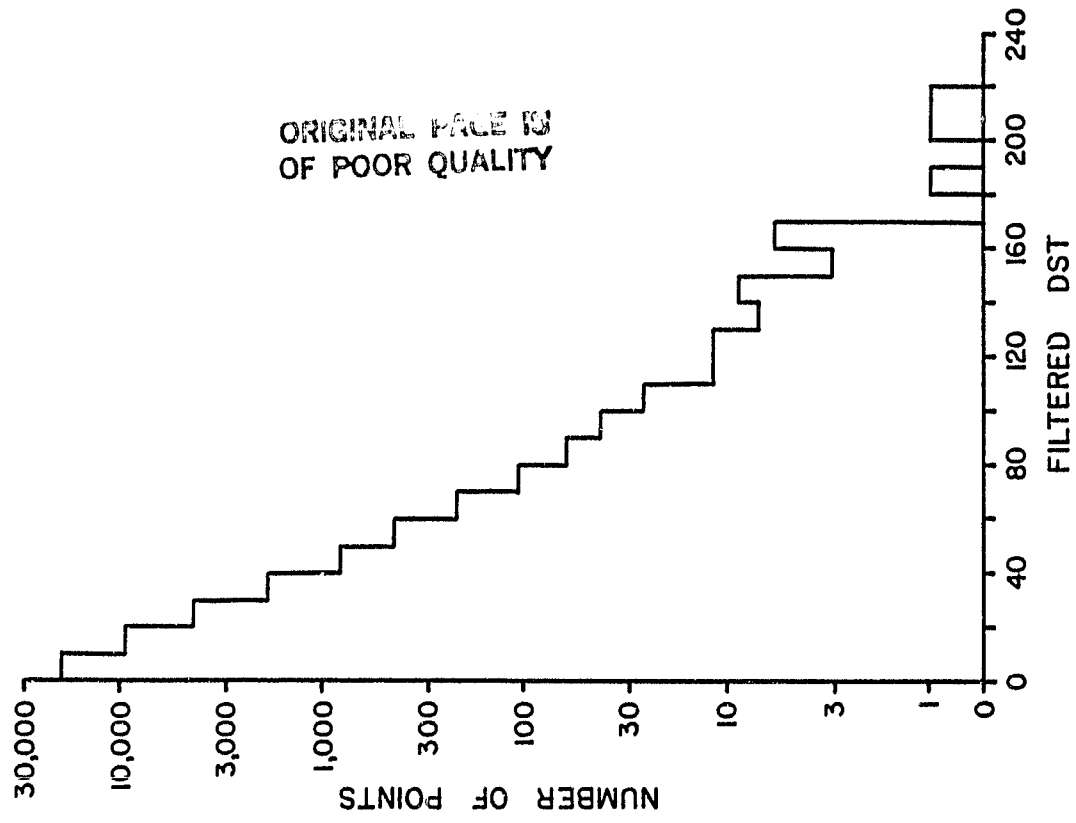
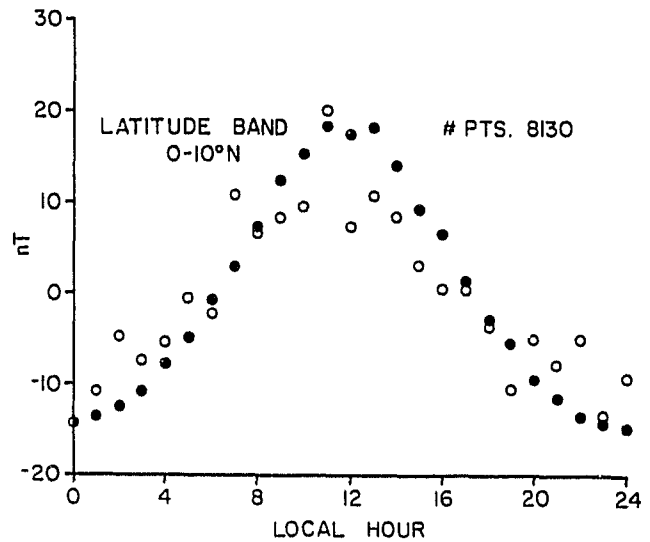
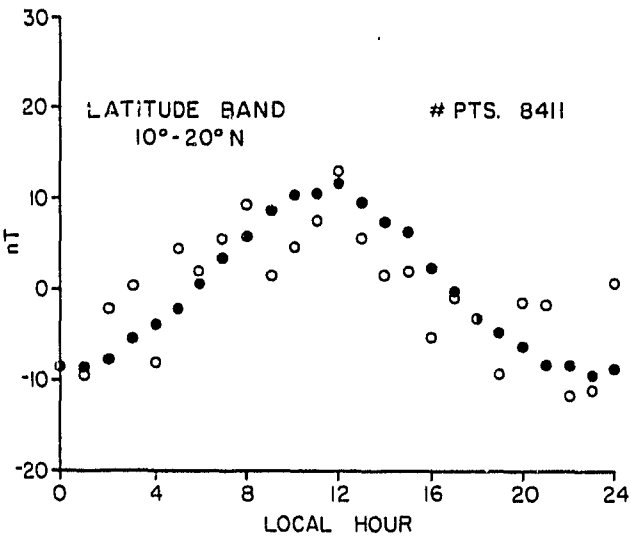
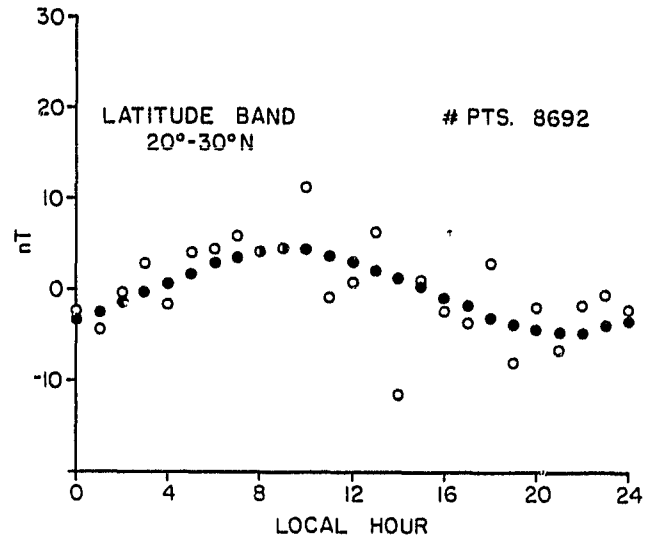
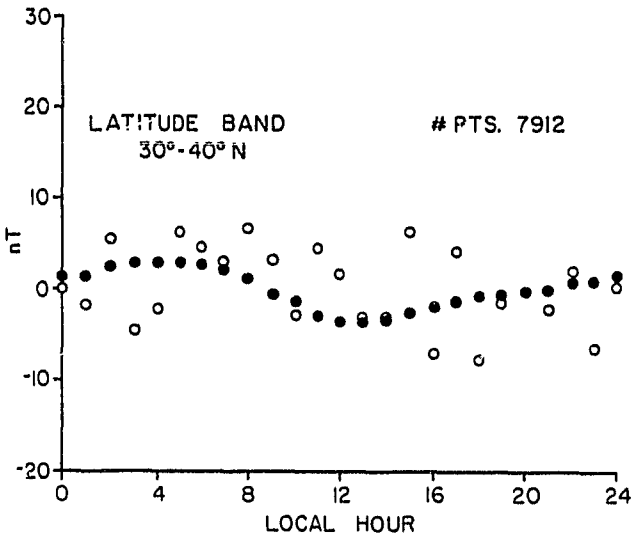
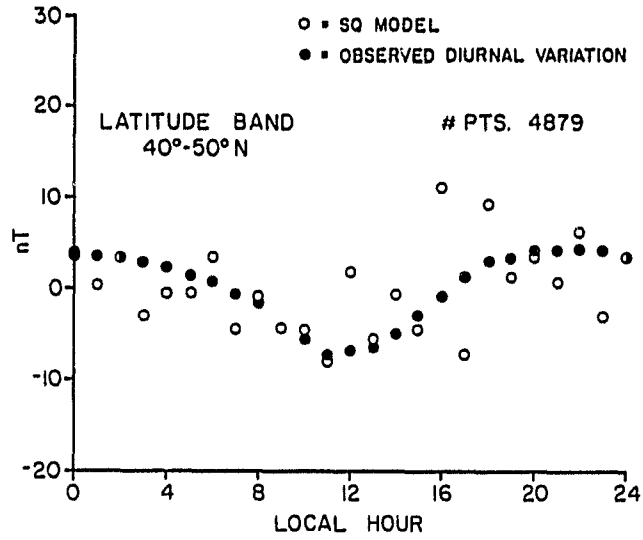


Figure 10

ORIGINAL PAGE IS
OF POOR QUALITY

Figure 11



ORIGINAL PAGE IS
OF POOR QUALITY

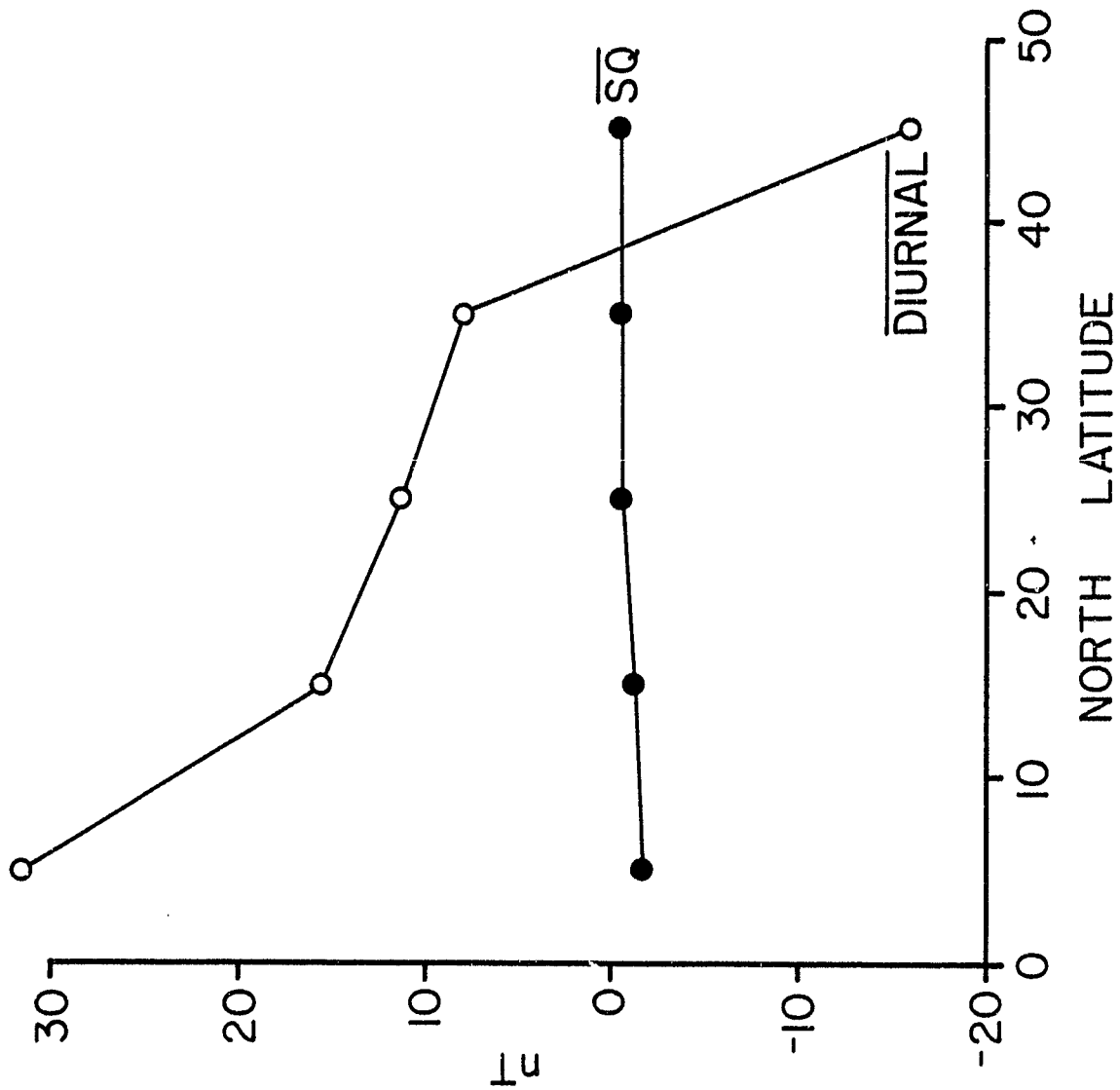


Figure 12

ORIGINAL PAGE IS
OF POOR QUALITY.

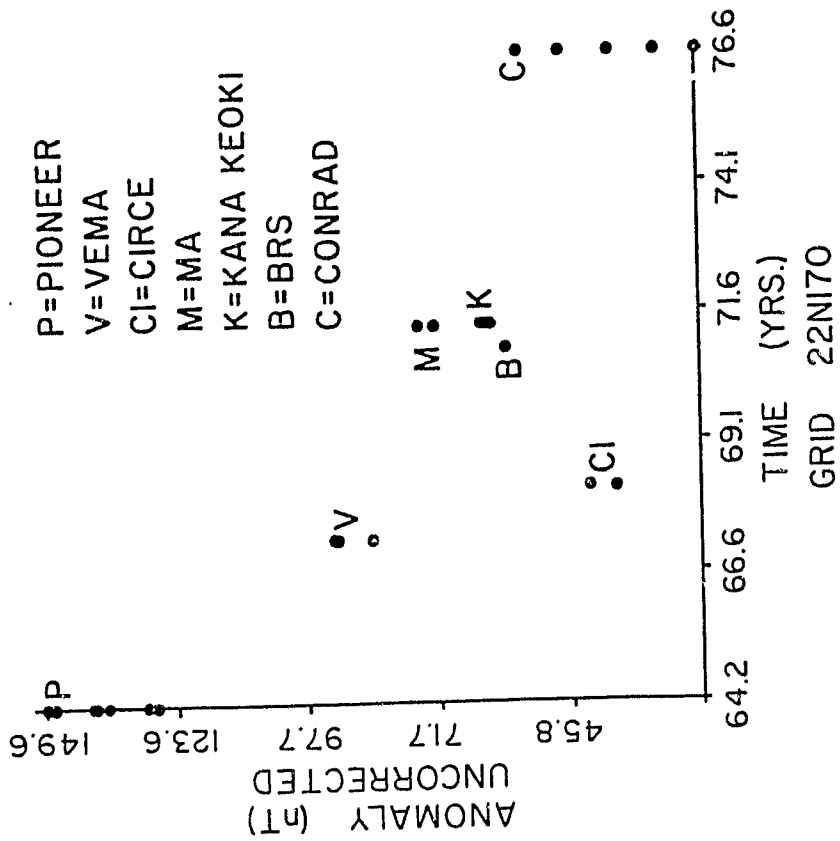
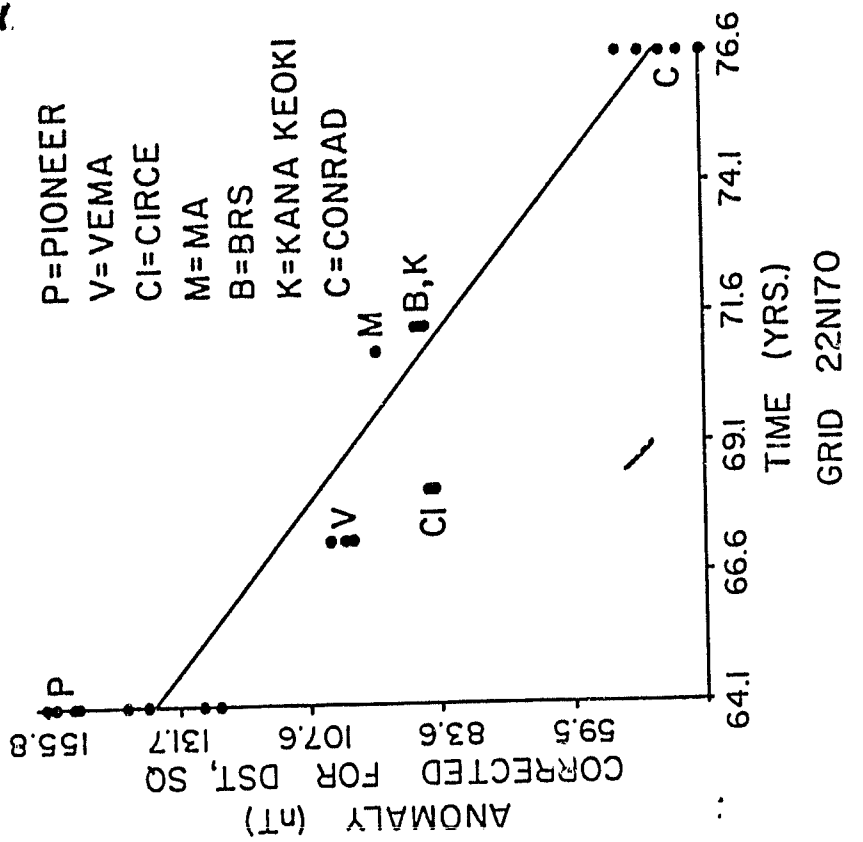
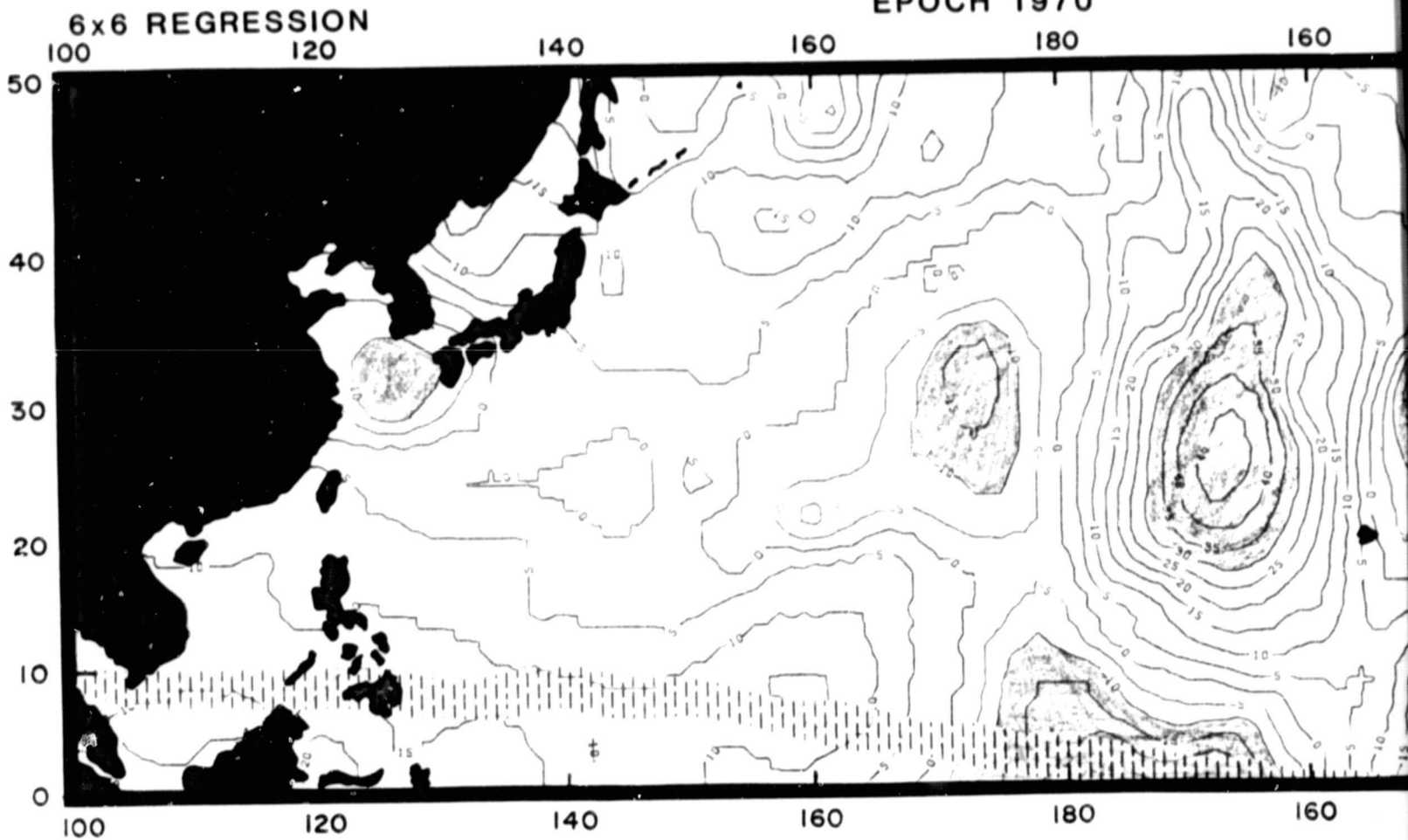


Figure 13

ORIGINAL PAGE
COLOR PHOTOGRAPH

SECULAR VARIATION ANOMALY

EPOCH 1970



< -10



-10 to 10



10 to 30

UNITS: nT/yr

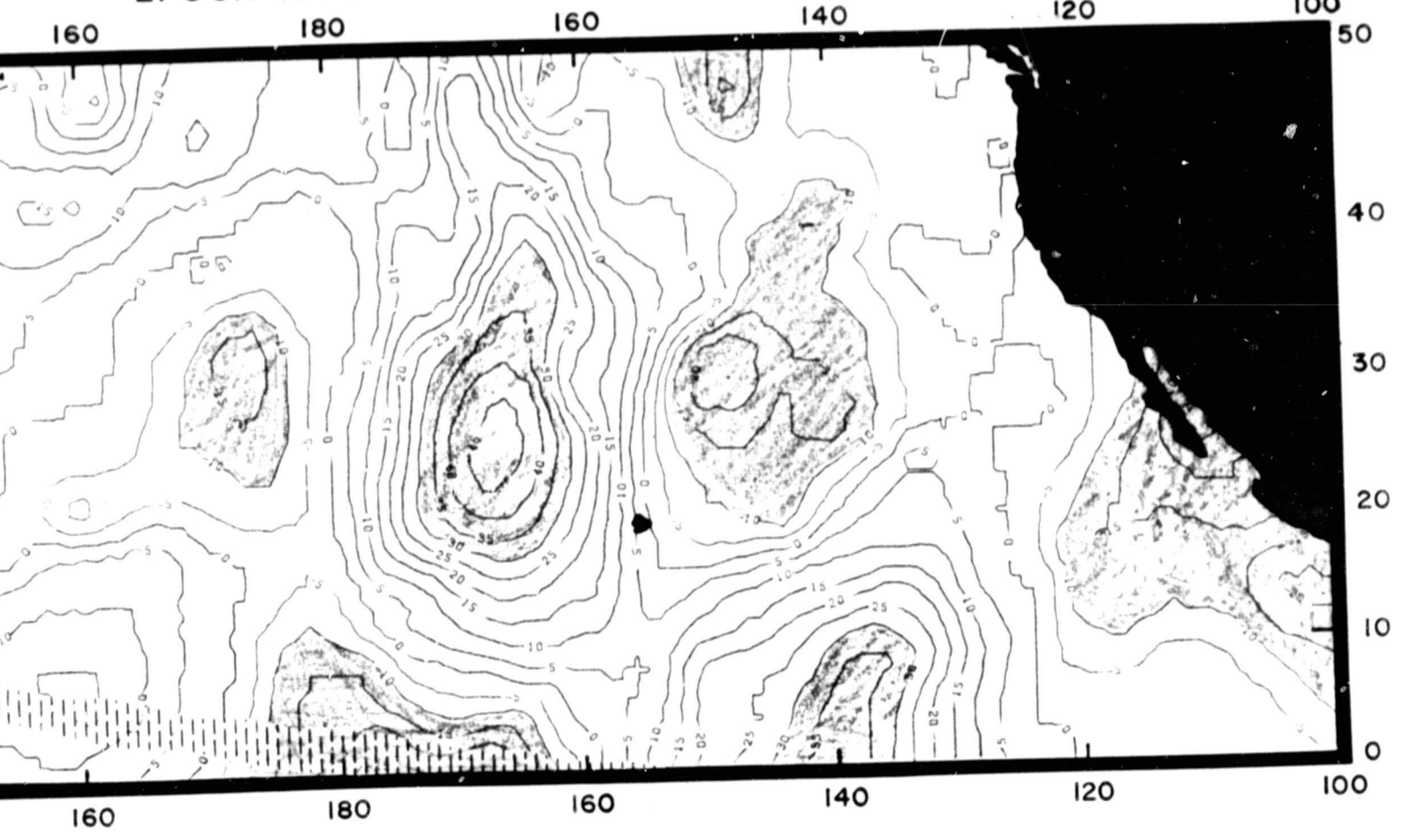
EOLDOUT FRAME

ORIGINAL PAGE
COLOR PHOTOGRAPH

R VARIATION ANOMALY

EPOCH 1970

REFERENCE PRMAG 1
120 100



○ -10 to 10 ○ 10 to 30 ⊗ > 30

UNITS: nT/yr

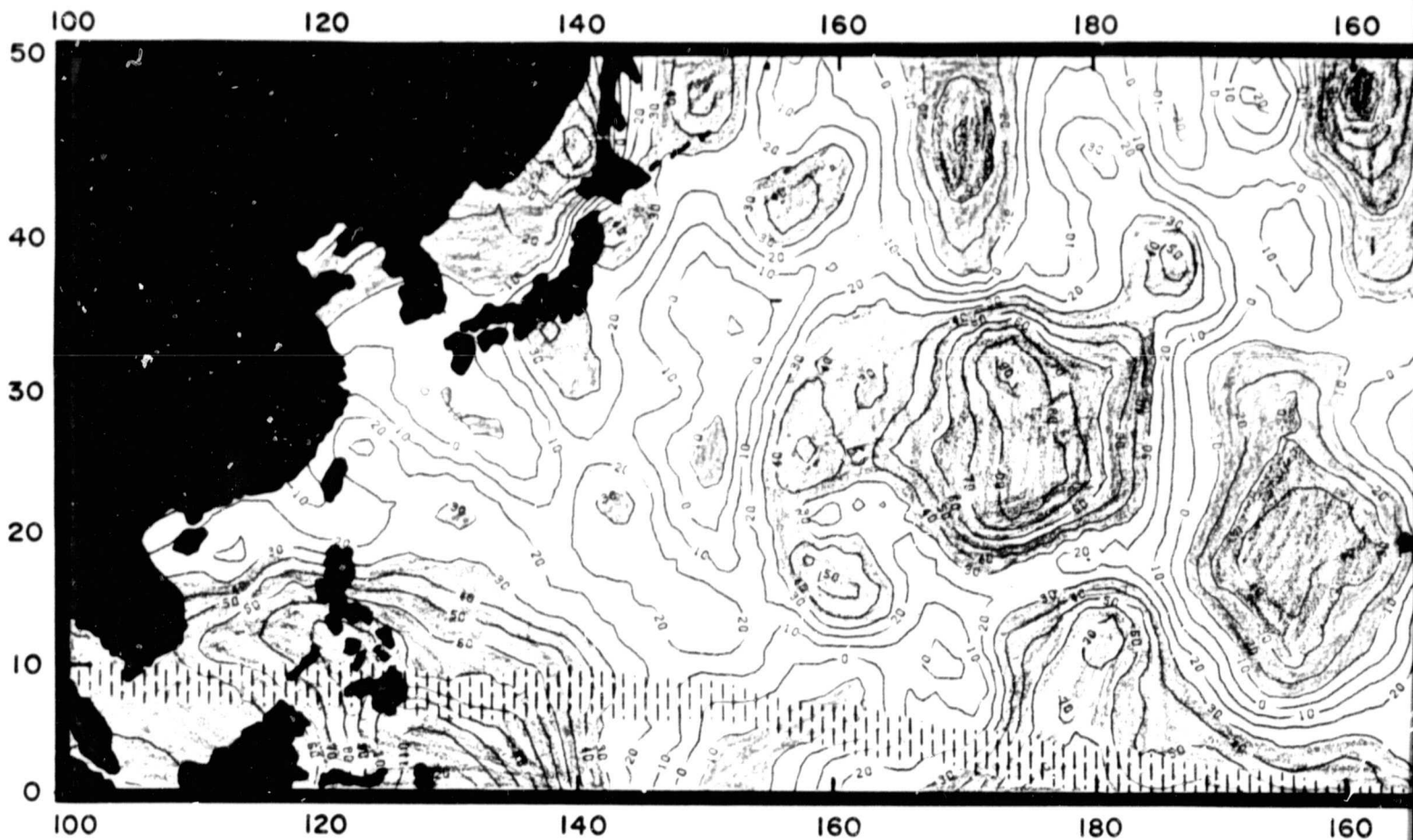
Figure 14

2 **SOLDOUT FRAME**

ORIGINAL PAGE
COLOR PHOTOGRAPH

FILTERED SEA SURFACE AND

6x6 REGRESSION



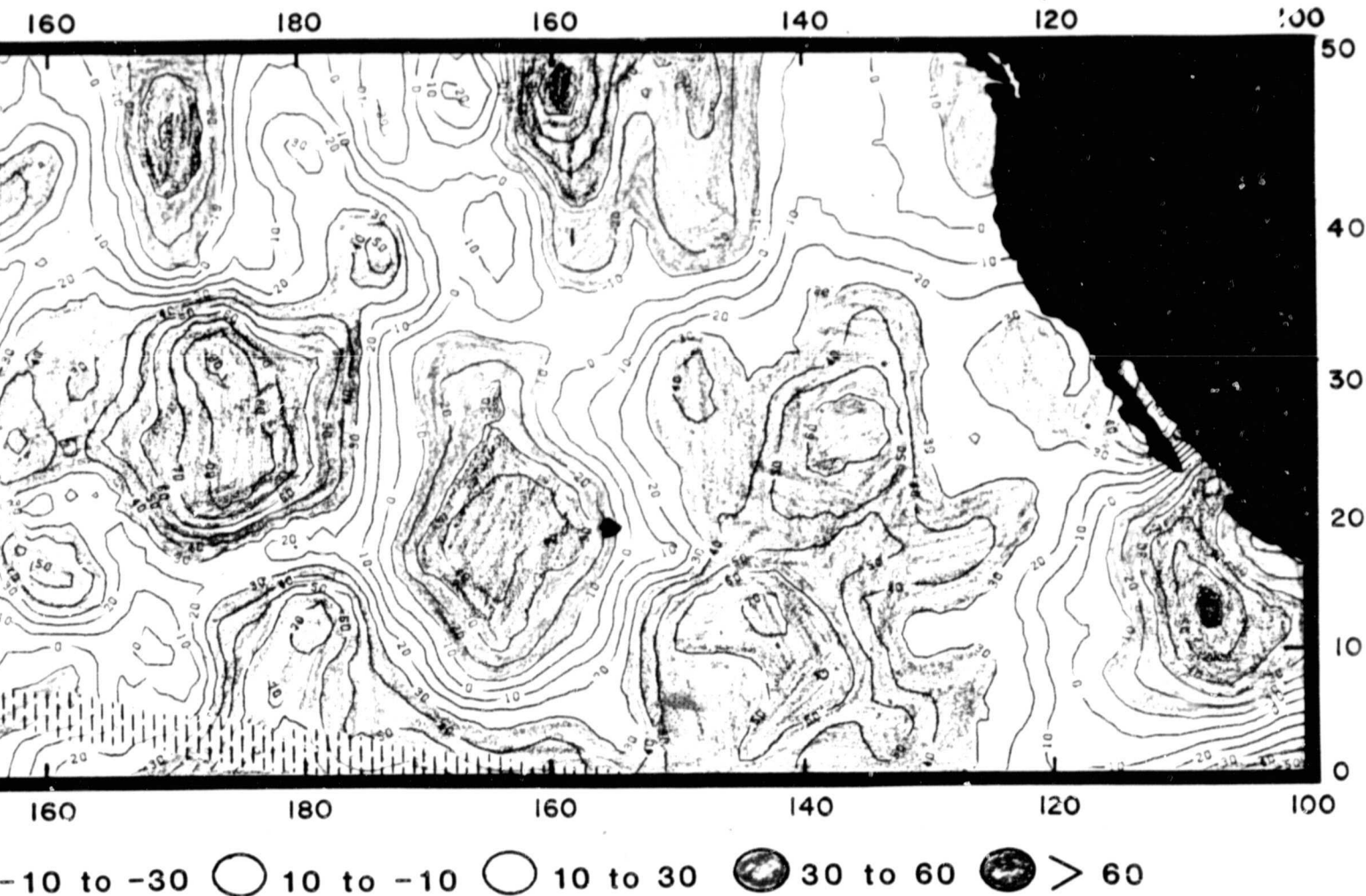
UNITS: nT

FOLDOUT FRAME

SEA SURFACE ANOMALY

ORIGINAL PAGE
COLOR PHOTOGRAPH

REFERENCE PRMAG 1



UNITS: nT

Figure 15

2 FOLDOUT FRAME

ORIGINAL PAGE IS
OF POOR QUALITY

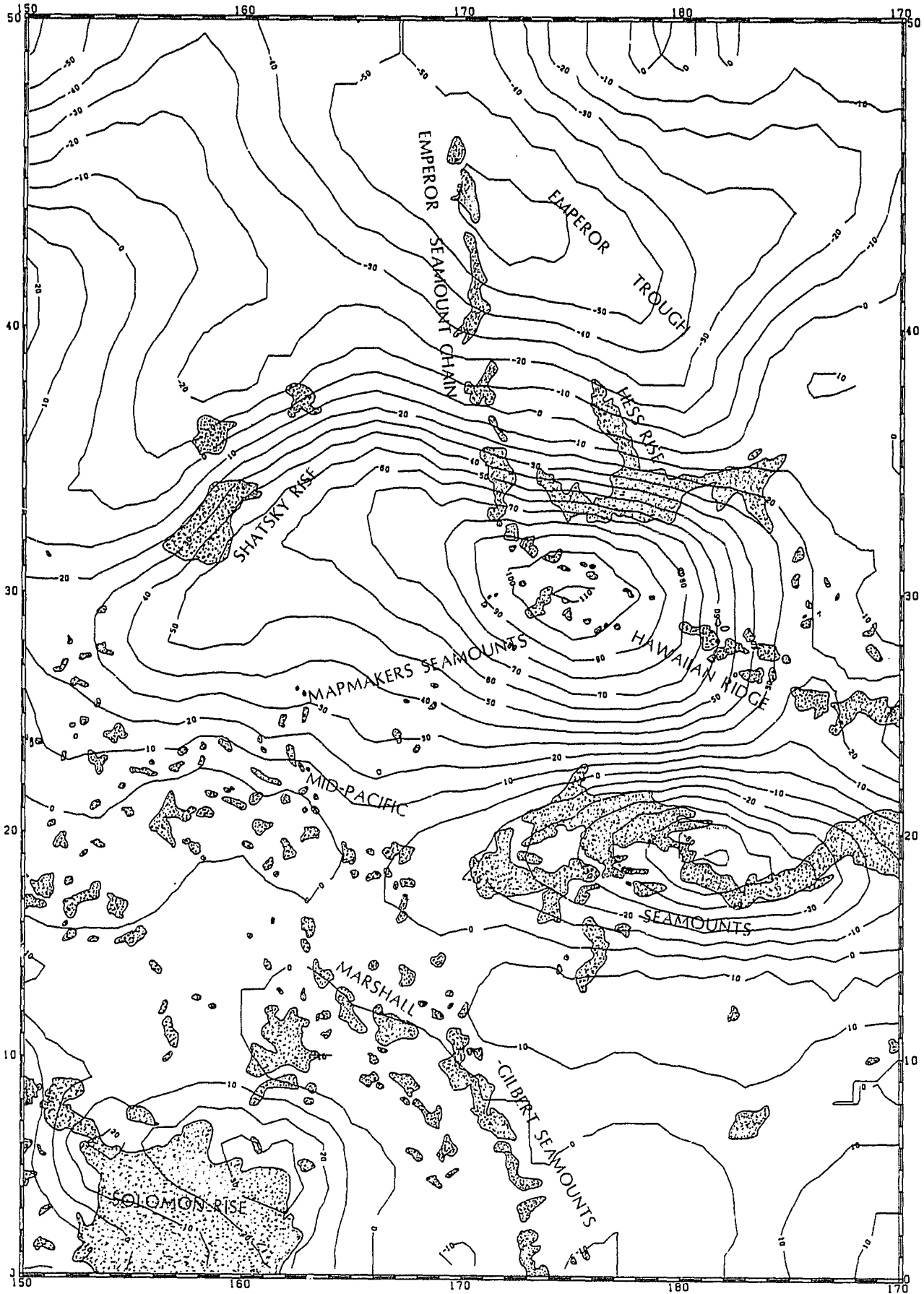
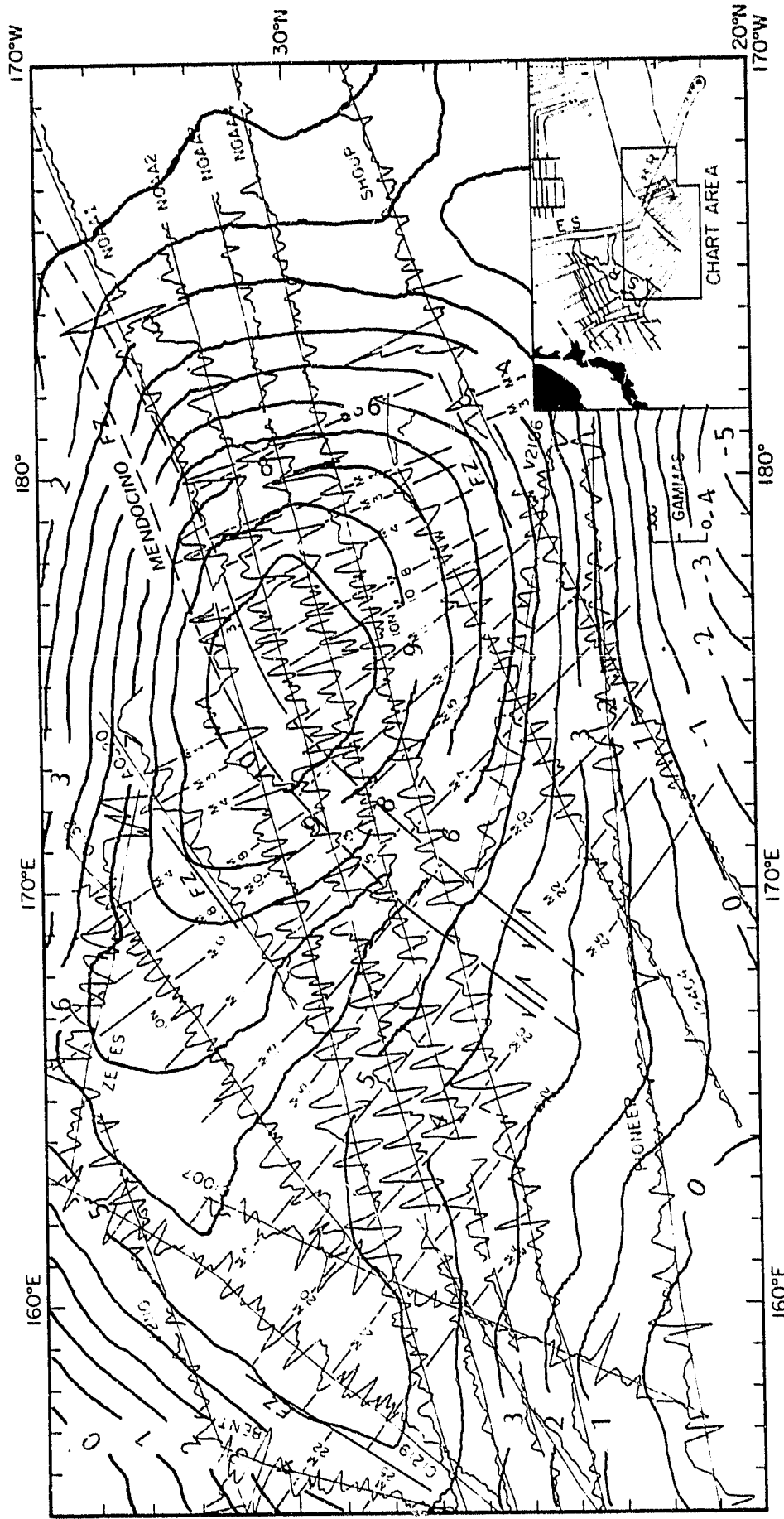


Figure 16

EMPEROR ANOMALY MAGSAT TOTAL FIELD ANOMALY



ORIGINAL PAGE IS
OF POOR QUALITY

Figure 18

ORIGINAL PAGE IS
OF POOR QUALITY

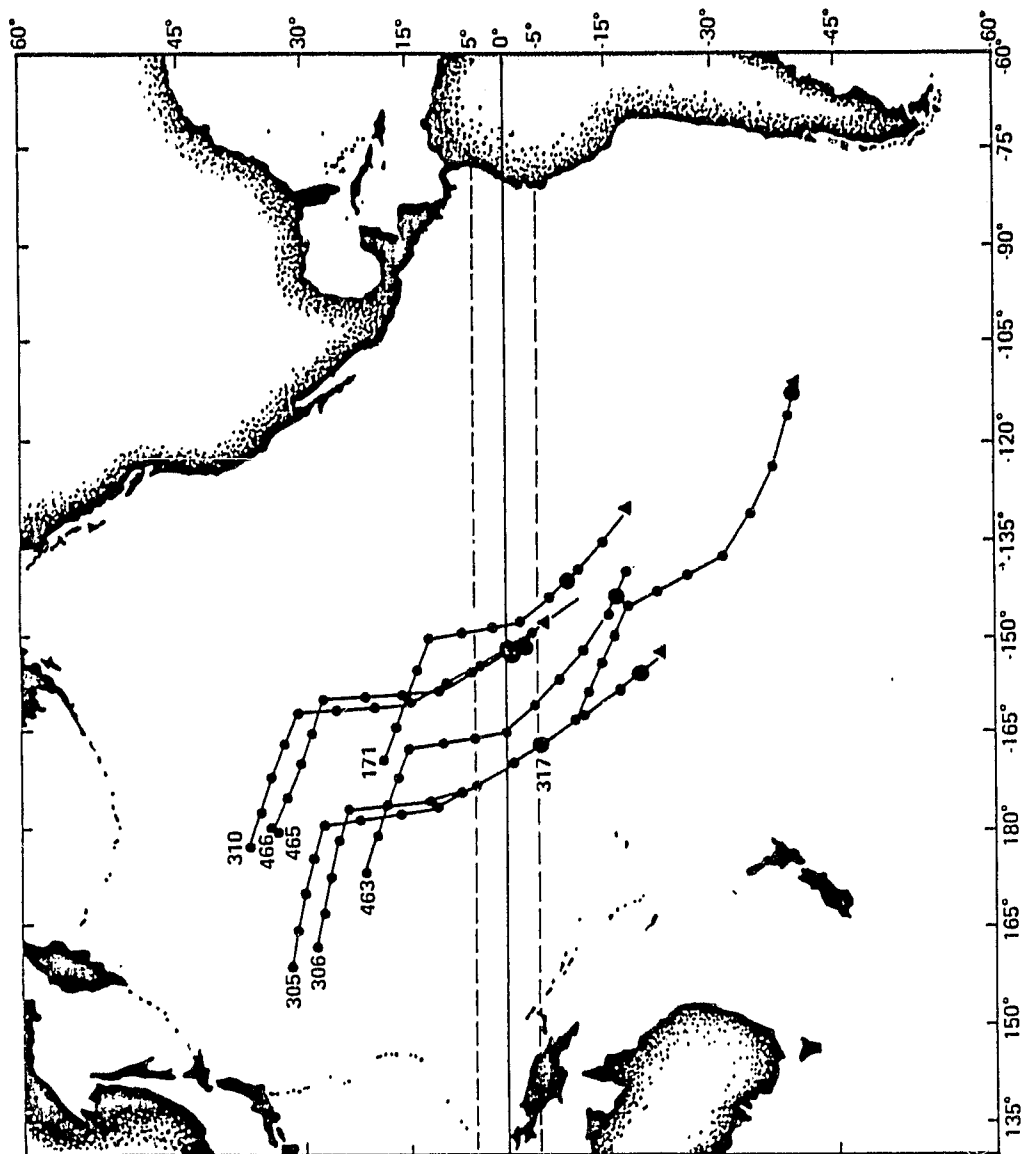
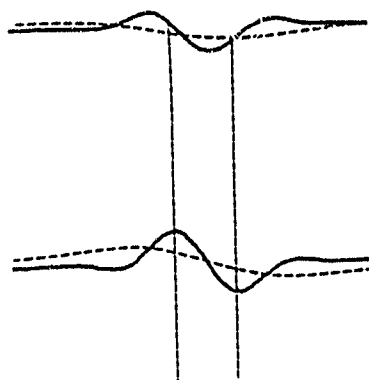


Figure 20

ORIGINAL PAGE IS
OF POOR QUALITY

SHATSKY RISE

AZZ: 315

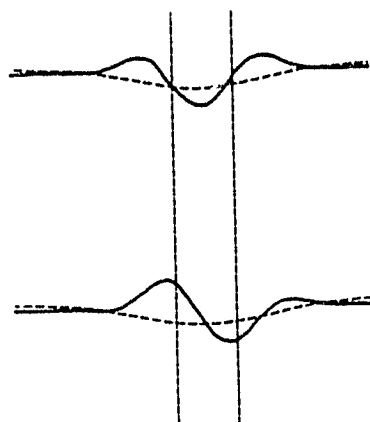


REMANENT

INDUCED

MARSHALL GILBERT
SMTS.

AZZ: 30

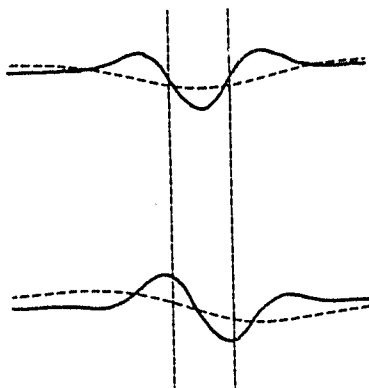


REMANENT

INDUCED

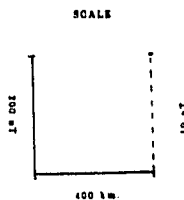
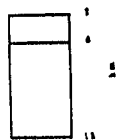
MID-PACIFIC SMTS.

AZZ: 0

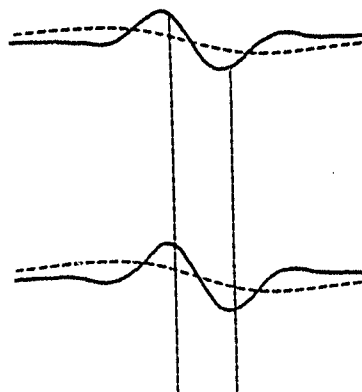


REMANENT

INDUCED

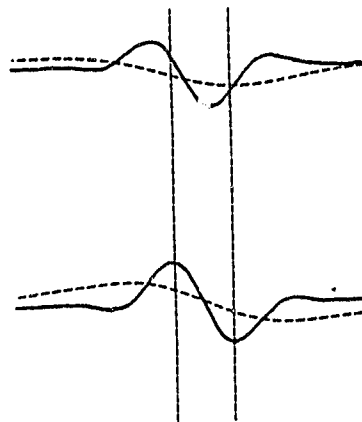


SCALE



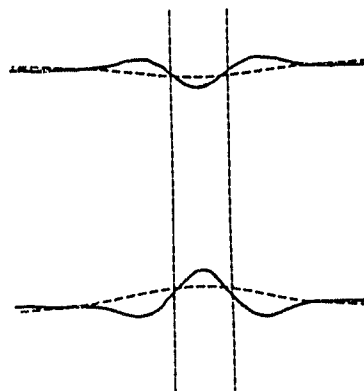
AZZ: 30

HAWAIIAN SMTS.



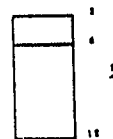
AZZ: 355

HESS RISE



AZZ: 90

EMPEROR SMTS.



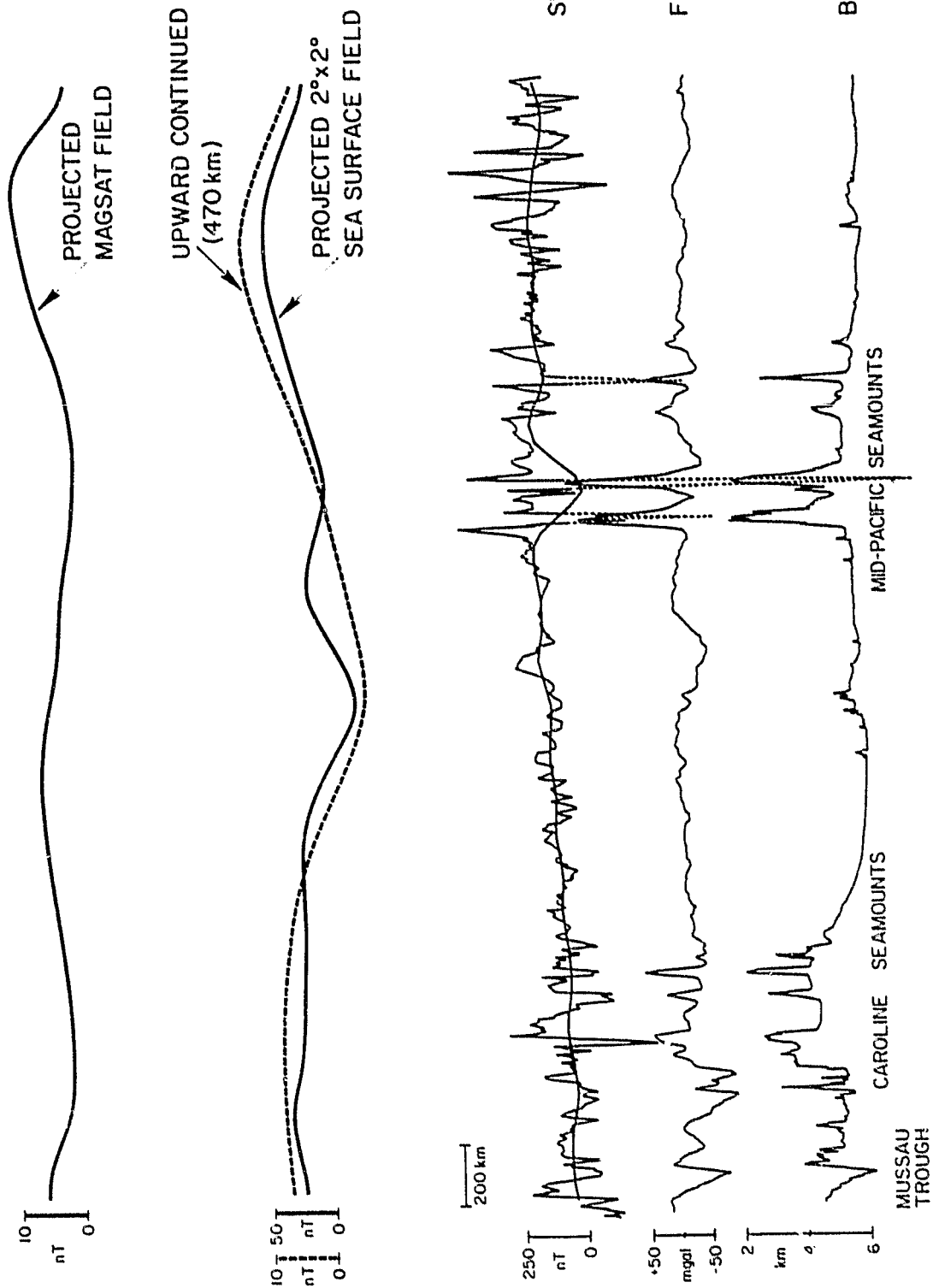


Figure 22

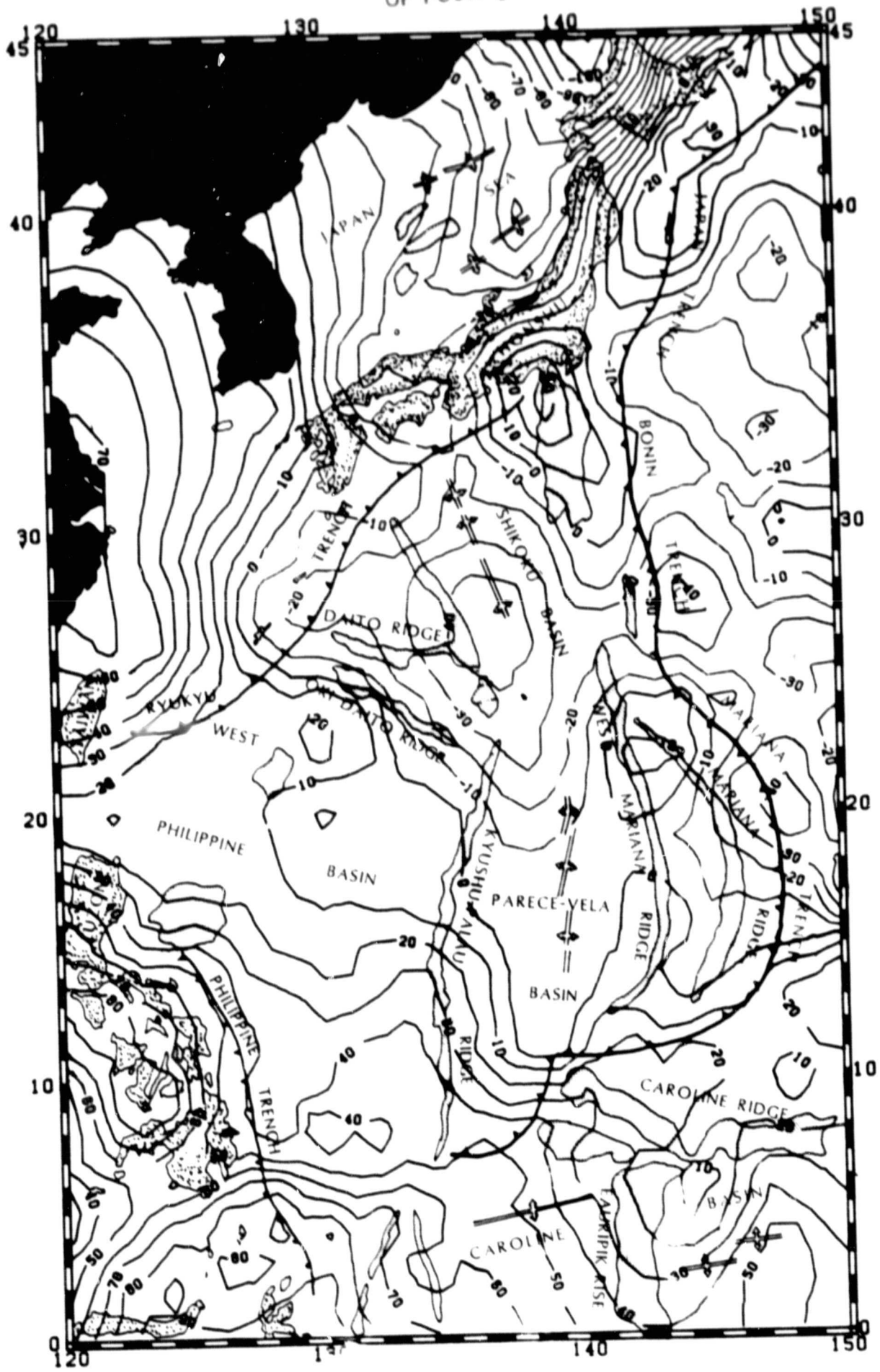


Figure 23

ORIGINAL PAGE IS
OF POOR QUALITY

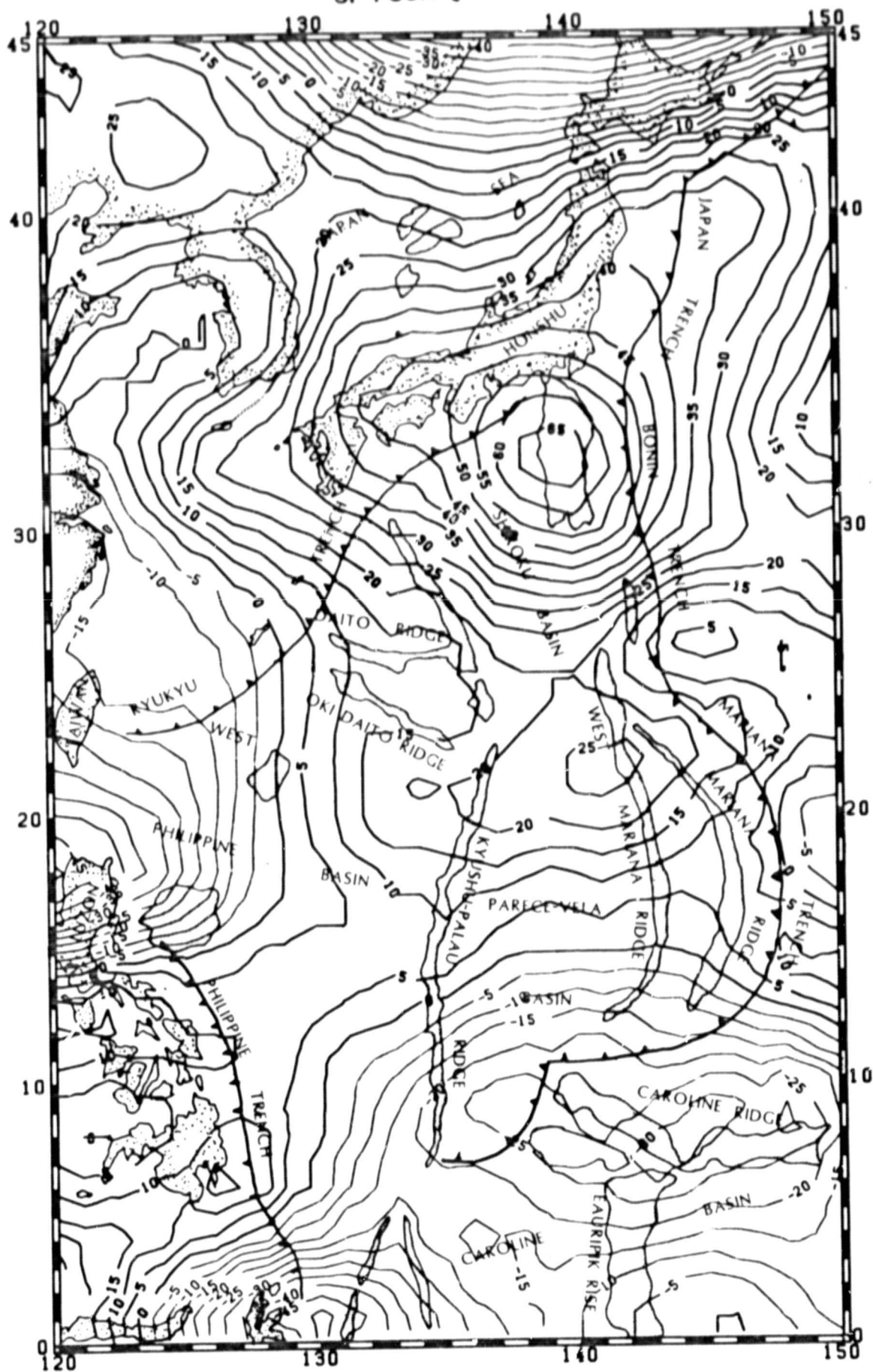


Figure 24

ORIGINAL PAGE IS
OF POOR QUALITY

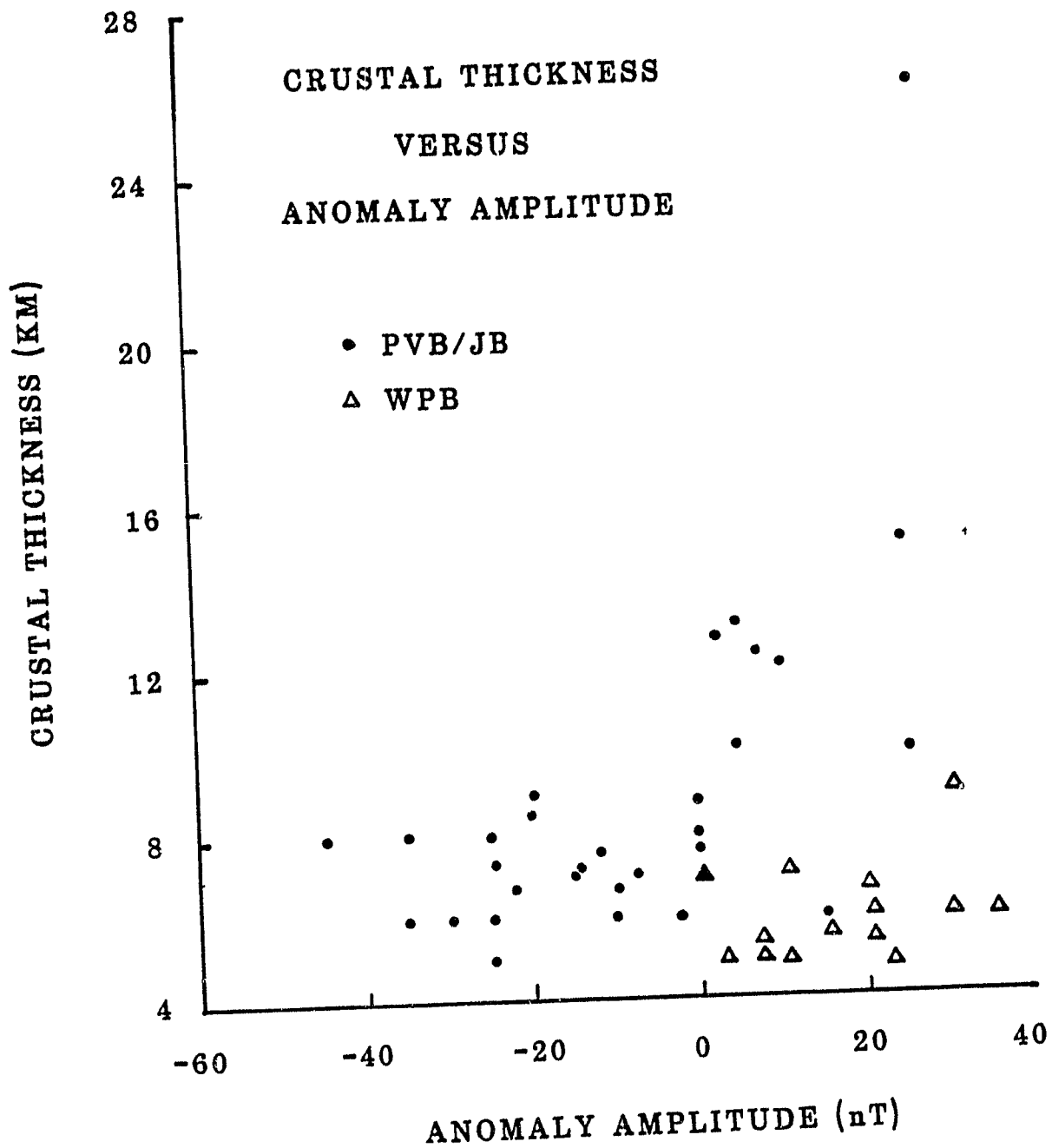


Figure 25a

HEAT FLOW VS ANOMALY AMPLITUDE

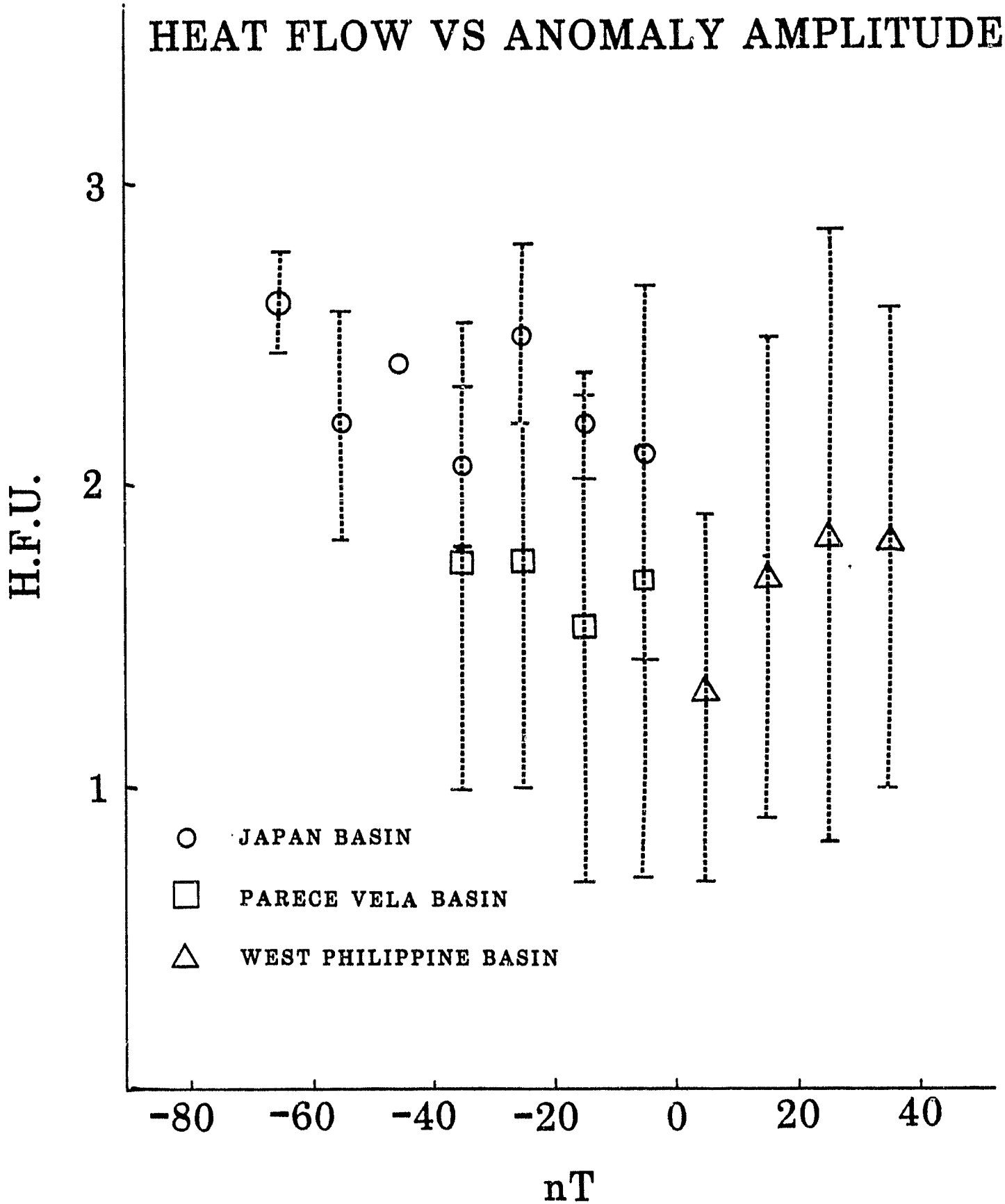


Figure 25 b

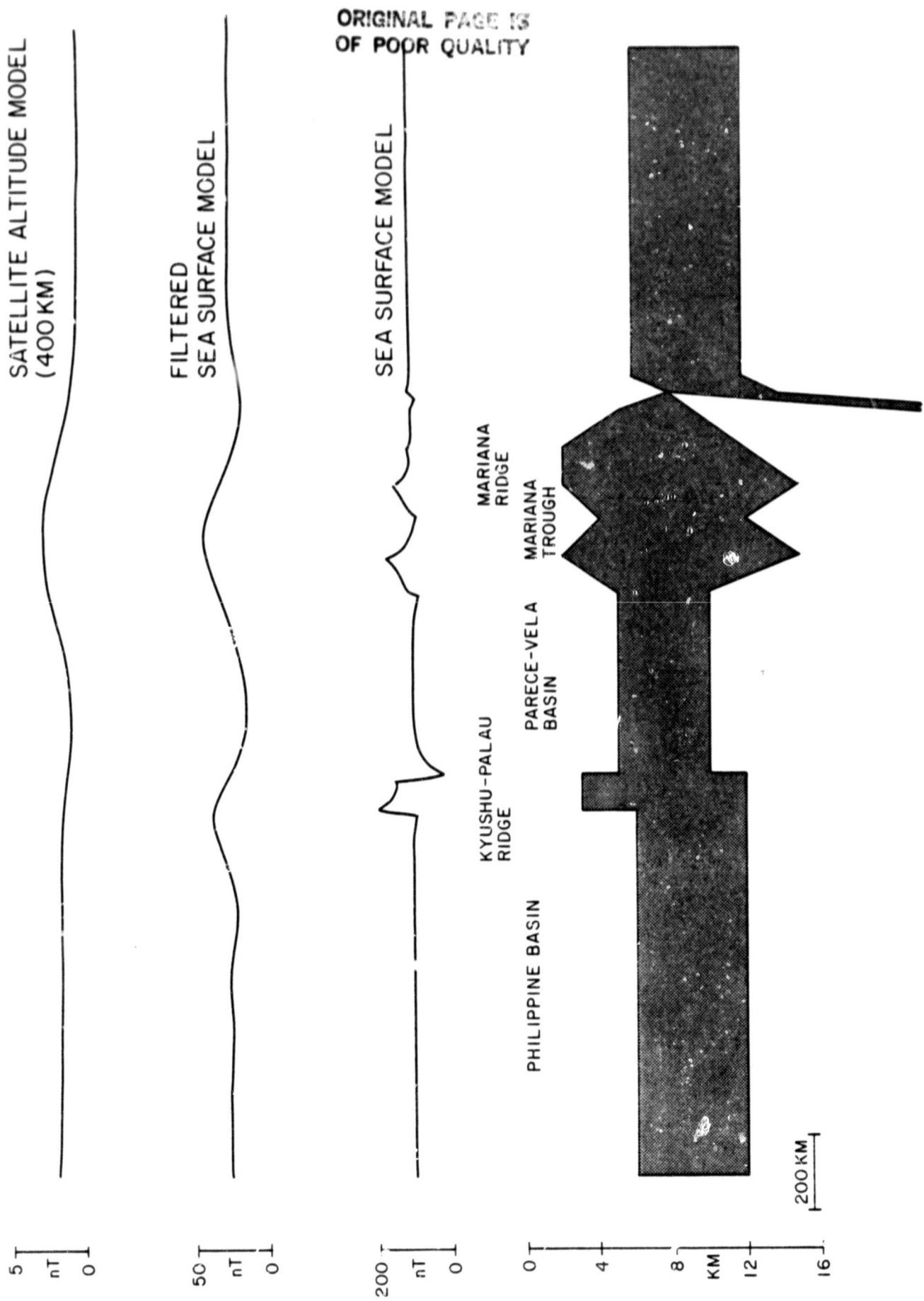


Figure 26

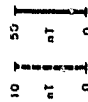
EASTERN PACIFIC

SOUTH

NORTH

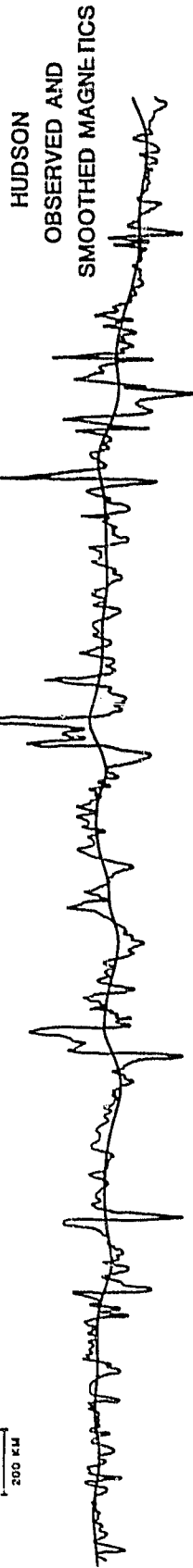


PROJECTED
MAGSAT FIELD



UPWARD CONTINUED
(400 KM)

PROJECTED 2X2
SEA SURFACE FIELD

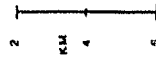


HUDSON

OBSERVED AND
SMOOTHED MAGNETICS



FREE-AIR GRAVITY



CLARION FZ

MOLOKAI FZ

MURRAY FZ

MENOCINO FZ

BATHYMETRY

ORIGINAL PRINT IS
OF POOR QUALITY

Figure 27

EASTERN PACIFIC

NORTH

SOUTH

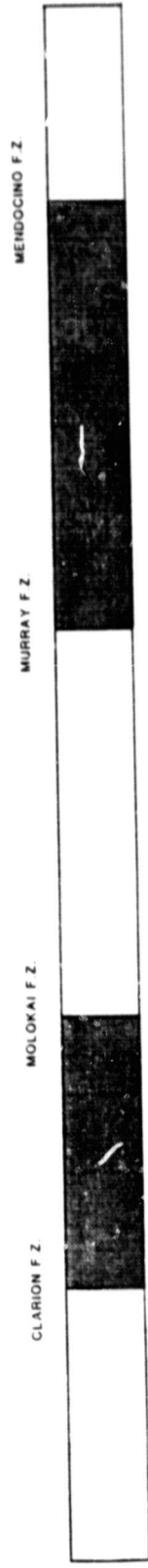
SATELLITE ALTITUDE MODEL
(400 KM)



FILTERED SEA LEVEL MODEL



SEA LEVEL MODEL



ORIGINAL PAGE IS
OF POOR QUALITY

Figure 28

Appendix A

Tracks and filter parameters used in the calculation of the sea surface intermediate wavelength anomaly field. Parameters and track ID's refer to LDGO program and data libraries.

882000	CC2R0003M	00	00	00	00	600	50	0	100	0	0.10	0
883000	CC2R0004M	00	00	00	00	600	50	0	100	0		
884000	CC2R0005M	00	00	00	00	600	50	0	100	0		
885000	CC2R0006M	00	00	00	00	600	50	0	100	0		
886000	CC2R0007M	00	00	00	00	600	50	0	100	0		
887000	CC2R0008M	00	00	00	00	600	50	0	100	0		
888000	CC2R0009M	00	00	00	00	600	50	0	100	0		
889000	CC2R0010M	00	00	00	00	600	50	0	100	0	0.10	0
890000	CC2R0011M	00	00	00	00	600	50	0	100	0		
891000	CC2R0012M	00	00	00	00	600	50	0	100	0		
892000	CC2R004M	00	00	00	00	600	50	0	100	0		
893000	CARRR1M	00	00	00	00	600	50	0	100	0		
894000	CARRR2M	00	00	00	00	600	50	0	100	0		
895000	CAT01M	00	00	00	00	600	50	0	100	0		
896000	CAT02M	00	00	00	00	600	50	0	100	0		
897000	CCCTW2M	00	00	00	00	600	50	0	100	0		
898000	CCCTW4M	00	00	00	00	600	50	0	100	0		
899000	CIRO2M	00	00	00	00	600	50	0	100	0	0.10	0
100000	CL751M	00	00	00	00	600	50	0	100	0		
101000	CL752M	00	00	00	00	600	50	0	100	0		
102000	CL753M	00	00	00	00	600	50	0	100	0		
103000	CL754M	00	00	00	00	600	50	0	100	0		
104000	CN006M	00	00	00	00	600	50	0	100	0		
105000	CN007M	00	00	00	00	600	50	0	100	0		
106000	CN011M	00	00	00	00	600	50	0	100	0		
107000	DD01AM	00	00	00	00	600	50	0	100	0		
108000	DPSN2M	00	00	00	00	600	50	0	100	0		
109000	EEL30M	00	00	00	00	600	50	0	100	0	0.10	0
110000	EEL31M	00	00	00	00	600	50	0	100	0	0.10	0
111000	ERDC2M	00	00	00	00	600	50	0	100	0	0.10	0
112000	GECS2M	00	00	00	00	600	50	0	100	0	0.10	0
113000	GECS3M	00	00	00	00	600	50	0	100	0	0.10	0
114000	GEFK M	00	00	00	00	600	50	0	100	0		
115000	GGLO7M	00	00	00	00	600	50	0	100	0	0.10	0
116000	GGLO8M	00	00	00	00	600	50	0	100	0		
117000	GGLO9M	00	00	00	00	600	50	0	100	0		
118000	GGLO16M	00	00	00	00	600	50	0	100	0		
119000	GGLO17M	00	00	00	00	600	50	0	100	0	0.10	0
120000	GGLO18M	00	00	00	00	600	50	0	100	0		
121000	GGLO19M	00	00	00	00	600	50	0	100	0	0.10	0
122000	GGLO20M	00	00	00	00	600	50	0	100	0	0.10	0
123000	GGLR2M	00	00	00	00	600	50	0	100	0		
124000	GGLR30M	00	00	00	00	600	50	0	100	0		
125000	GGLR31M	00	00	00	00	600	50	0	100	0		
126000	GGLR32M	00	00	00	00	600	50	0	100	0	0.10	0
127000	GGLR33M	00	00	00	00	600	50	0	100	0		
128000	GGLR54M	00	00	00	00	600	50	0	100	0		
129000	GGLR55M	00	00	00	00	600	50	0	100	0	0.10	0
130000	GGLR56M	00	00	00	00	600	50	0	100	0		
131000	GGLR57M	00	00	00	00	600	50	0	100	0		
132000	GGLR58M	00	00	00	00	600	50	0	100	0		
133000	GGLR59M	00	00	00	00	600	50	0	100	0		
134000	GGLR60M	00	00	00	00	600	50	0	100	0		
135000	GGLR61M	00	00	00	00	600	50	0	100	0		
136000	GGLR62M	00	00	00	00	600	50	0	100	0	0.10	0
137000	GGLR63M	00	00	00	00	600	50	0	100	0		
138000	GGLR64M	00	00	00	00	600	50	0	100	0		
139000	GGLR65M	00	00	00	00	600	50	0	100	0		
140000	GGLR67M	00	00	00	00	600	50	0	100	0		
141000	QUAY1M	00	00	00	00	600	50	0	100	0		
142000	QUAY2M	00	00	00	00	600	50	0	100	0		
143000	QUAY3M	00	00	00	00	600	50	0	100	0		
144000	IHAKUM	00	00	00	00	600	50	0	100	0	0.10	0
145000	IIL3AM	00	00	00	00	600	50	0	100	0		
146000	IIL3BM	00	00	00	00	600	50	0	100	0		
147000	HT001M	00	00	00	00	600	50	0	100	0		
148000	HT002M	00	00	00	00	600	50	0	100	0		
149000	HT003M	00	00	00	00	600	50	0	100	0		
150000	HT05BM	00	00	00	00	600	50	0	100	0	0.10	0
151000	HT05CM	00	00	00	00	600	50	0	100	0		
152000	HT05DM	00	00	00	00	600	50	0	100	0		
153000	HT669M	00	00	00	00	600	50	0	100	0		
154000	HT869M	00	00	00	00	600	50	0	100	0		
155000	HU140M	00	00	00	00	600	50	0	100	0		
156000	HU145M	00	00	00	00	600	50	0	100	0		
157000	HU150M	00	00	00	00	600	50	0	100	0		
158000	HU155M	00	00	00	00	600	50	0	100	0		
159000	IGU01M	00	00	00	00	600	50	0	100	0		
160000	IGU04M	00	00	00	00	600	50	0	100	0		
161000	IGU05M	00	00	00	00	600	50	0	100	0		
162000	IID0EM	00	00	00	00	600	50	0	100	0		

ORIGINAL PAGE IS
OF POOR QUALITY

16300	IID03M	00	00	00	00	600	50.	0	100.	00	00	00
16400	IID04M	00	00	00	00	600	50.	0	100.	00	00	00
16500	INDP1M	00	00	00	00	600	50.	0	100.	00	00	00
16600	INDP2M	00	00	00	00	600	50.	0	100.	00	00	00
16700	INDP3M	00	00	00	00	600	50.	0	100.	00	00	00
16800	INDP4M	00	00	00	00	600	50.	0	100.	00	00	00
16900	JD06 M	00	00	00	00	600	50.	0	100.	00	00	00
17000	JD08 M	00	00	00	00	600	50.	0	100.	00	00	00
17100	JD7A M	00	00	00	00	600	50.	0	100.	00	00	00
17200	JPYN2M	00	00	00	00	600	50.	0	100.	00	00	00
17300	JPYN4M	00	00	00	00	600	50.	0	100.	00	00	00
17400	K7112M	00	00	00	00	600	50.	0	100.	00	00	00
17500	KH683M	00	00	00	00	600	50.	0	100.	00	00	00
17600	KH84AM	00	00	00	00	600	50.	0	100.	00	00	00
17700	KH84DM	00	00	00	00	600	50.	0	100.	00	00	00
17800	KK711M	00	00	00	00	600	50.	0	100.	00	00	00
17900	KK712M	00	00	00	00	600	50.	0	100.	00	00	00
18000	KK721M	00	00	00	00	600	50.	0	100.	00	00	00
18100	KK728M	00	00	00	00	600	50.	0	100.	00	00	00
18200	KK72AM	00	00	00	00	600	50.	0	100.	00	00	00
18300	KK730M	00	00	00	00	600	50.	0	100.	00	00	00
18400	KK741M	00	00	00	00	600	50.	0	100.	00	00	00
18500	KK746M	00	00	00	00	600	50.	0	100.	00	00	00
18600	KK747M	00	00	00	00	600	50.	0	100.	00	00	00
18700	KK748M	00	00	00	00	600	50.	0	100.	00	00	00
18800	KK750M	00	00	00	00	600	50.	0	100.	00	00	00
18900	KK760M	00	00	00	00	600	50.	0	100.	00	00	00
19000	KK762M	00	00	00	00	600	50.	0	100.	00	00	00
19100	KK76AM	00	00	00	00	600	50.	0	100.	00	00	00
19200	KK76BM	00	00	00	00	600	50.	0	100.	00	00	00
19300	KK771M	00	00	00	00	600	50.	0	100.	00	00	00
19400	KK772M	00	00	00	00	600	50.	0	100.	00	00	00
19500	KK773M	00	00	00	00	600	50.	0	100.	00	00	00
19600	KK774M	00	00	00	00	600	50.	0	100.	00	00	00
19700	KK775M	00	00	00	00	600	50.	0	100.	00	00	00
19800	KKH01M	00	00	00	00	600	50.	0	100.	00	00	00
19900	LUS7BM	00	00	00	00	600	50.	0	100.	00	00	00
20000	MA680M	00	00	00	00	600	50.	0	100.	00	00	00
20100	MA701M	00	00	00	00	600	50.	0	100.	00	00	00
20200	MA702M	00	00	00	00	600	50.	0	100.	00	00	00
20300	MA703M	00	00	00	00	600	50.	0	100.	00	00	00
20400	MA704M	00	00	00	00	600	50.	0	100.	00	00	00
20500	MA705M	00	00	00	00	600	50.	0	100.	00	00	00
20600	MARA4M	00	00	00	00	600	50.	0	100.	00	00	00
20700	MMAP M	00	00	00	00	600	50.	0	100.	00	00	00
20800	MNSN1M	00	00	00	00	600	50.	0	100.	00	00	00
20900	MSNO1M	00	00	00	00	600	50.	0	100.	00	00	00
21000	MNO1AM	00	00	00	00	600	50.	0	100.	00	00	00
21100	NNO6HM	00	00	00	00	600	50.	0	100.	00	00	00
21200	NOV1AM	00	00	00	00	600	50.	0	100.	00	00	00
21300	NOV2AM	00	00	00	00	600	50.	0	100.	00	00	00
21400	NOVA1M	00	00	00	00	600	50.	0	100.	00	00	00
21500	NOVA2M	00	00	00	00	600	50.	0	100.	00	00	00
21600	NOVA3M	00	00	00	00	600	50.	0	100.	00	00	00
21700	NOVA3M	00	00	00	00	600	50.	0	100.	00	00	00
21800	NOVA9M	00	00	00	00	600	50.	0	100.	00	00	00
21900	NVA10M	00	00	00	00	600	50.	0	100.	00	00	00
22000	OWENS5M	00	00	00	00	600	50.	0	100.	00	00	00
22100	P6365M	00	00	00	00	600	50.	0	100.	00	00	00
22200	P6501M	00	00	00	00	600	50.	0	100.	00	00	00
22300	P6829M	00	00	00	00	600	50.	0	100.	00	00	00
22400	P6971M	00	00	00	00	600	50.	0	100.	00	00	00
22500	P7004M	00	00	00	00	600	50.	0	100.	00	00	00
22600	P7008M	00	00	00	00	600	50.	0	100.	00	00	00
22700	P7103M	00	00	00	00	600	50.	0	100.	00	00	00
22800	P7201M	00	00	00	00	600	50.	0	100.	00	00	00
22900	P7304M	00	00	00	00	600	50.	0	100.	00	00	00
23000	PI064M	00	00	00	00	600	50.	0	100.	00	00	00
23100	PIQ01M	00	00	00	00	600	50.	0	100.	00	00	00
23200	PP001M	00	00	00	00	600	50.	0	100.	00	00	00
23300	PP008M	00	00	00	00	600	50.	0	100.	00	00	00
23400	PP01AM	00	00	00	00	600	50.	0	100.	00	00	00
23500	PP01BM	00	00	00	00	600	50.	0	100.	00	00	00
23600	PP25AM	00	00	00	00	600	50.	0	100.	00	00	00
23700	PP25BM	00	00	00	00	600	50.	0	100.	00	00	00
23800	PP25CM	00	00	00	00	600	50.	0	100.	00	00	00
23900	PP25DM	00	00	00	00	600	50.	0	100.	00	00	00
24000	PP25EM	00	00	00	00	600	50.	0	100.	00	00	00
24100	PP25FM	00	00	00	00	600	50.	0	100.	00	00	00
24200	PP25GM	00	00	00	00	600	50.	0	100.	00	00	00
24300	PP29AM	00	00	00	00	600	50.	0	100.	00	00	00
	PP29CM	00	00	00	00	600	50.	0	100.	00	00	00

24400	PP290DM	0	0	0	0	600	50.	0	100.	0
24500	PP294EM	0	0	0	0	600	50.	0	100.	0
24600	PP299FM	0	0	0	0	600	50.	0	100.	0
24700	PP29GM	0	0	0	0	600	50.	0	100.	0
24800	PP301M	0	0	0	0	600	50.	0	100.	0
24900	PP304M	0	0	0	0	600	50.	0	100.	0
25000	PP623M	0	0	0	0	600	50.	0	100.	0
25100	PP71AM	0	0	0	0	600	50.	0	100.	0
25200	PP71BM	0	0	0	0	600	50.	0	100.	0
25300	PP71CM	0	0	0	0	600	50.	0	100.	0
25400	PPISAM	0	0	0	0	600	50.	0	100.	0
25500	PPI6WM	0	0	0	0	600	50.	0	100.	0
25600	PPIOFM	0	0	0	0	600	50.	0	100.	0
25700	PPIONM	0	0	0	0	600	50.	0	100.	0
25800	PRDA4M	0	0	0	0	600	50.	0	100.	0
25900	RRFO1 M	0	0	0	0	600	50.	0	100.	0
26000	RRISE1M	0	0	0	0	600	50.	0	100.	0
26100	RRFEHOM	0	0	0	0	600	50.	0	100.	0
26200	SCAN2M	0	0	0	0	600	50.	0	100.	0
26300	SCAN3M	0	0	0	0	600	50.	0	100.	0
26400	SCAN4M	0	0	0	0	600	50.	0	100.	0
26500	SCAN5M	0	0	0	0	600	50.	0	100.	0
26600	SDT13M	0	0	0	0	600	50.	0	100.	0
26700	SSCA4M	0	0	0	0	600	50.	0	100.	0
26800	SSHOPM	0	0	0	0	600	50.	0	100.	0
26900	SSUC5DM	0	0	0	0	600	50.	0	100.	0
27000	SSU6WM	0	0	0	0	600	50.	0	100.	0
27100	SSU7WM	0	0	0	0	600	50.	0	100.	0
27200	STX01M	0	0	0	0	600	50.	0	100.	0
27300	STX02M	0	0	0	0	600	50.	0	100.	0
27400	STX06M	0	0	0	0	600	50.	0	100.	0
27500	STX08M	0	0	0	0	600	50.	0	100.	0
27600	STX09M	0	0	0	0	600	50.	0	100.	0
27700	STX10M	0	0	0	0	600	50.	0	100.	0
27800	SV370M	0	0	0	0	600	50.	0	100.	0
27900	SV970M	0	0	0	0	600	50.	0	100.	0
28000	SWAN1M	0	0	0	0	600	50.	0	100.	0
28100	TSDD03M	0	0	0	0	600	50.	0	100.	0
28200	TSDD05M	0	0	0	0	600	50.	0	100.	0
28300	TSDD07M	0	0	0	0	600	50.	0	100.	0
28400	TTRA3M	0	0	0	0	600	50.	0	100.	0
28500	UM63 M	0	0	0	0	600	50.	0	100.	0
28600	UM642M	0	0	0	0	600	50.	0	100.	0
28700	UM66AM	0	0	0	0	600	50.	0	100.	0
28800	UM66DM	0	0	0	0	600	50.	0	100.	0
28900	UM67 M	0	0	0	0	600	50.	0	100.	0
29000	UM69 M	0	0	0	0	600	50.	0	100.	0
29100	V1815M	0	0	0	0	600	50.	0	100.	0
29200	V1907M	0	0	0	0	600	50.	0	100.	0
29300	V1908M	0	0	0	0	600	50.	0	100.	0
29400	V1909M	0	0	0	0	600	50.	0	100.	0
29500	V20003M	0	0	0	0	600	50.	0	100.	0
29600	V20004M	0	0	0	0	600	50.	0	100.	0
29700	V20005M	0	0	0	0	600	50.	0	100.	0
29800	V20006M	0	0	0	0	600	50.	0	100.	0
29900	V20007M	0	0	0	0	600	50.	0	100.	0
30000	V20008M	0	0	0	0	600	50.	0	100.	0
30100	V22104M	0	0	0	0	600	50.	0	100.	0
30200	V22105M	0	0	0	0	600	50.	0	100.	0
30300	V22106M	0	0	0	0	600	50.	0	100.	0
30400	V22107M	0	0	0	0	600	50.	0	100.	0
30500	V22108M	0	0	0	0	600	50.	0	100.	0
30600	V22110M	0	0	0	0	600	50.	0	100.	0
30700	V22112M	0	0	0	0	600	50.	0	100.	0
30800	V22113M	0	0	0	0	600	50.	0	100.	0
30900	V221A9M	0	0	0	0	600	50.	0	100.	0
31000	V221B9M	0	0	0	0	600	50.	0	100.	0
31100	V22403M	0	0	0	0	600	50.	0	100.	0
31200	V22404M	0	0	0	0	600	50.	0	100.	0
31300	V22405M	0	0	0	0	600	50.	0	100.	0
31400	V22406M	0	0	0	0	600	50.	0	100.	0
31500	V22407M	0	0	0	0	600	50.	0	100.	0
31600	V22809M	0	0	0	0	600	50.	0	100.	0
31700	V228B10M	0	0	0	0	600	50.	0	100.	0
31800	V228B11M	0	0	0	0	600	50.	0	100.	0
31900	V228B13M	0	0	0	0	600	50.	0	100.	0
32000	V228B14M	0	0	0	0	600	50.	0	100.	0
32100	V228B15M	0	0	0	0	600	50.	0	100.	0
32200	V228B16M	0	0	0	0	600	50.	0	100.	0
32300	V228B17M	0	0	0	0	600	50.	0	100.	0
32400	V228B18M	0	0	0	0	600	50.	0	100.	0

322500	V2819M	0	0	0	600	50.	0	100.	0
322600	V2901M	0	0	0	600	50.	0	100.	0
322700	V3209M	0	0	0	600	50.	0	100.	0
322800	V3210M	0	0	0	600	50.	0	100.	0
322900	V3211M	0	0	0	600	50.	0	100.	0
323000	V3212M	0	0	0	600	50.	0	100.	0
323100	V3213M	0	0	0	600	50.	0	100.	0.10 0
323200	V3214M	0	0	0	600	50.	0	100.	0.10 0
323300	V3303M	0	0	0	600	50.	0	100.	0
323400	V3308M	0	0	0	600	50.	0	100.	0
323500	V3309M	0	0	0	600	50.	0	100.	0
323600	V3310M	0	0	0	600	50.	0	100.	0
323700	V3311M	0	0	0	600	50.	0	100.	0
323800	V3312M	0	0	0	600	50.	0	100.	0
323900	V3313M	0	0	0	600	50.	0	100.	0
324000	V3401M	0	0	0	600	50.	0	100.	0
324100	V3402M	0	0	0	600	50.	0	100.	0
324200	V3403M	0	0	0	600	50.	0	100.	0
324300	V3404M	0	0	0	600	50.	0	100.	0
324400	V3405M	0	0	0	600	50.	0	100.	0
324500	V3503M	0	0	0	600	50.	0	100.	0
324600	V3504M	0	0	0	600	50.	0	100.	0
324700	V3505M	0	0	0	600	50.	0	100.	0
324800	V3506M	0	0	0	600	50.	0	100.	0
324900	V3603M	0	0	0	600	50.	0	100.	0
325000	V3604M	0	0	0	600	50.	0	100.	0
325100	V3605M	0	0	0	600	50.	0	100.	0
325200	V3606M	0	0	0	600	50.	0	100.	0
325300	V3607M	0	0	0	600	50.	0	100.	0
325400	V3608M	0	0	0	600	50.	0	100.	0
325500	V3609M	0	0	0	600	50.	0	100.	0
325600	V3610M	0	0	0	600	50.	0	100.	0
325700	V3611M	0	0	0	600	50.	0	100.	0
325800	V3612M	0	0	0	600	50.	0	100.	0.10 0
325900	V3613M	0	0	0	600	50.	0	100.	0
326000	V3614M	0	0	0	600	50.	0	100.	0
326100	V3616M	0	0	0	600	50.	0	100.	0
326200	VAL16M	0	0	0	600	50.	0	100.	0
326300	YQ715M	0	0	0	600	50.	0	100.	0
326400	YQ733M	0	0	0	600	50.	0	100.	0
326500	ZTES3M	0	0	0	600	50.	0	100.	0.10 0
326600	ZTS04M	0	0	0	600	50.	0	100.	0
326700	ZTS05M	0	0	0	600	50.	0	100.	0.10 0
326800	ZTS06M	0	0	0	600	50.	0	100.	0
326900	ZTS07M	0	0	0	600	50.	0	100.	0
327000	ZTS28M	0	0	0	600	50.	0	100.	0.10 0
327100	ZTS68M	0	0	0	600	50.	0	100.	0

ORIGINAL PAGE IS
OF POOR QUALITY

APPENDIX B

Subroutine FIELDG and the associated Pre-Magsat coefficients
used in the generation of the Pre-Magsat reference Field.

```

C*****
SUBROUTINE FIELDG (DLAT, DLONG, ALT, TM, NMX, L, X, Y, Z, F)
C      MODIFIED JULY 22, 1981
C      FOR DOCUMENTATION OF THIS SUBROUTINE AND SUBROUTINE FIELD SEE :
C      NATIONAL SPACE SCIENCE DATA CENTER'S PUBLICATION
C      COMPUTATION OF THE MAIN GEOMAGNETIC FIELD FROM
C      SPHERICAL HARMONIC EXPANSIONS
C      DATA USERS' NOTE, NSSDC 68-11, MAY 1968
C      GODDARD SPACE FLIGHT CENTER, GREENBELT, MD.
      EQUIVALENCE (SHMIT(1,1), TG(1,1))
      COMMON NDPY(3), LPYR(4), JBSYR
      COMMON /COEFFS/TG(18,18), G(18,18), GT(18,18), GTT(18,18), TLAST
      1, TZERO
      COMMON /FLDCOM/ST, CT, SPH, CPH, R, NMAX, BT, BP, BR, B
      DIMENSION AID(11), SHMIT(18,18)
      DATA A/O./
      A=6378.16
      FLAT=1. -1./298.25
      A2=A**2
      A4=A**4
      B2=(A*FLAT)**2
      A2B2=A2*(1.-FLAT**2)
      A4B4=A4*(1.-FLAT**4)
C*****IF L.LE.0 DON'T READ COEFFICIENTS FILE
      IF (L) 1,1,2
C*****IF DATE IS THE SAME AS LAST DON'T UPDATE COEFFICIENTS
1      IF (TM-TLAST) 17,19,17
C*****READ FIELD COEFFICIENTS
2      READ (3,3) J, K, TZERO, (AID(I), I=1, 11)
3      FORMAT (2I1, 1X, F6.1, 10A6, A3)
      L=0
4      FORMAT (2I3, 5X6HEPOCH=, F7.1, 5X10A6, A3)
      MAXN=0
      TEMP=0.
5      READ (3,6,END=74) N, M, GNM, HNM, GTNM, HTNM, GTTNM, HTTNM
      WRITE(5,6) N, M, GNM, HNM, GTNM, HTNM, GTTNM, HTTNM
6      FORMAT (2I3, 6F11.4)
      IF (N.LE.0) GOTO74
      MAXN=(MAX0(N, MAXN))
      G(N,M)=GNM
      GT(N,M)=GTM
      GTT(N,M)=GTTM
      IF (M.EQ.1) GOTO5
      G(M-1,N)=HNM
      GT(M-1,N)=HTNM
      GTT(M-1,N)=HTTNM
      GO TO 5
74      CONTINUE
C*****WRITE COEFFICIENTS FOR DEBUGGING PURPOSES
D7      WRITE (5,8)
D8      FORMAT (6HO N M, 6X1HG, 10X1HH, 9X2HGT, 9X2HHT, 8X3HGTT8X3HHTT//)
D      WRITE(5,239)MAXN
D239     FORMAT(I10)
D      DO 12 N=2, MAXN
D      DO 12 M=1, N
D      MI=M-1
D      IF (M.EQ.1) GO TO 10
D      WRITE (5,9) N, M, G(N,M), G(MI,N), GT(N,M), GT(MI,N), GTT(N,M), GTT(MI,N)
D9      FORMAT (2I3, 6F11.4)
D      GO TO 12
D10     WRITE (5,11) N, M, G(N,M), GT(N,M), GTT(N,M)
D11     FORMAT (2I3, F11.4, 11X, F11.4, 11XF11.4)
D12     CONTINUE
C*****K.NE.0 IF COEFFICIENTS ARE GAUSS QUASINORMALIZED
C*****K.EQ.0 IF COEFFICIENTS ARE SCHMIDT QUASINORMALIZED
14      IF (K.NE.0) GOTO17
      SHMIT(1,1)=-1.
      DO 15 N=2, MAXN
      SHMIT(N,1)=SHMIT(N-1,1)*FLOAT(2*N-3)/FLOAT(N-1)
      SHMIT(1,N)=0.
      JJ=2
      DO 15 M=2, N
      SHMIT(N,M)=SHMIT(N,M-1)*SQRT(FLOAT((N-M+1)*JJ)/FLOAT(N+M-2))
      SHMIT(M-1,N)=SHMIT(N,M)
15      JJ=1
      DO 16 N=2, MAXN
      DO 16 M=1, N
      G(N,M)=G(N,M)*SHMIT(N,M)
      GT(N,M)=GT(N,M)*SHMIT(N,M)
      GTT(N,M)=GTT(N,M)*SHMIT(N,M)
      IF (M.EQ.1) GOTO16

```

```

G(M-1,N)=G(M-1,N)*SHMIT(M-1,N)
GT(M-1,N)=GT(M-1,N)*SHMIT(M-1,N)
GTT(M-1,N)=GTT(M-1,N)*SHMIT(M-1,N)
16 CONTINUE
17 T=TM-TZERO
DO 18 N=1,MAXN
DO 18 M=1,N
TG(N,M)=G(N,M)+T*(GT(N,M)+GTT(N,M)*T)
C*****BE CAREFUL THAT SECULAR ACCELERATION TERMS ARE DEFINED AS
C***** A*T/2.
IF (M.EQ.1) GOTO18
TG(M-1,N)=G(M-1,N)+T*(GT(M-1,N)+GTT(M-1,N)*T)
18 CONTINUE
TLAST=TM
19 DLATR=DLAT/57.2957795
SINLA=SIN(DLATR)
RLONG=DLONG/57.2957795
CPH=COS(RLONG)
SPH=SIN(RLONG)
IF (J.EQ.0) GOTO20
C*****IF J.NE.0 OUTPUT IS IN GEOCENTRIC COORDINATES
R=ALT+6371.0
CT=SINLA
GO TO 21
C*****CALCULATE GEODETIC CONSTANTS
20 SINLA2=SINLA**2
COSLA2=1.-SINLA2
DEN2=A2-A2B2*SINLA2
DEN=SQRT(DEN2)
FAC=((ALT*DEN)+A2)/((ALT*DEN)+B2)**2
CT=SINLA/SQRT(FAC*COSLA2+SINLA2)
R=SQRT(ALT*(ALT+2.*DEN)+(A4-A4B4*SINLA2)/DEN2)
21 ST=SQRT(1.-CT**2)
C*****EVALUATE SPHERICAL HARMONIC TO ORDER AND DEGREE NMAX (NOTE:
C*****NMAX IS N+1 OF MATH EXPRESSION I.E. NMAX 14=DEGREE 13 TO
C*****SATISFY THE COMPUTER DO LOOPS
NMAX=MINO(NMX,MAXN)
C*****EVALUATE SPHERICAL HARMONICS
CALL FIELD
Y=BP
F=B
IF (J) 22,23,22
22 X=-BT
Z=-BR
RETURN
C TRANSFORMS FIELD TO GEODETIC DIRECTIONS
23 SIND=SINLA*ST-SQRT(COSLA2)*CT
COSD=SQRT(1.0-SIND**2)
X=-BT*COSD-BR*SIND
Z=BT*SIND-BR*COSD
D WRITE(5,1212)DLAT,DLONG,TM,X,Y,Z,F
1212 FORMAT(7F8.1)
RETURN
END
SUBROUTINE FIELD
COMMON NDPY(3),LPYR(4),JBSYR
COMMON/COEFFS/G(18,18),GX(18,18),GT(18,18),GTT(18,18),TLAST
1,TZERO
COMMON/FLDCOM/ST,CT,SPH,CPH,R,NMAX,BT,BP,BR,B
DIMENSION P(18,18),DP(18,18),CONST(18,18),SP(18),CP(18),FN(18),
1FM(18)
IF (P(1,1).EQ.1.0) GO TO 3
1 P(1,1)=1.
DP(1,1)=0.
SP(1)=0.
CP(1)=1.
DO 2 N=2,18
FN(N)=N
DO 2 M=1,N
FM(M)=M-1
2 CONST(N,M)=FLOAT((N-2)**2-(M-1)**2)/FLOAT((2*N-3)*(2*N-5))
3 SP(2)=SPH
CP(2)=CPH
DO 4 M=3,NMAX
SP(M)=SP(2)*CP(M-1)+CP(2)*SP(M-1)
4 CP(M)=CP(2)*CP(M-1)-SP(2)*SP(M-1)
AOR=6371.2/R
AR=AOR**2
BT=0.
BP=0.
BR=0.

```

ORIGINAL PAGE
OF POOR QUALITY

```

DO 8 N=2,NMAX
AR=AOR*AR
DO 8 M=1,N
IF (N-M) 6,5,6
5 P(N,N)=ST*P(N-1,N-1)
DP(N,N)=ST*DP(N-1,N-1)+CT*P(N-1,N-1)
GO TO 7
6 P(N,M)=CT*P(N-1,M)-CONST(N,M)*P(N-2,M)
DP(N,M)=CT*DP(N-1,M)-ST*P(N-1,M)-CONST(N,M)*DP(N-2,M)
7 PAR=P(N,M)*AR
IF (M.EQ.1) GO TO 9
TEMP=G(N,M)*CP(M)+G(M-1,N)*SP(M)
BP=BP-(G(N,M)*SP(M)-G(M-1,N)*CP(M))*FM(M)*PAR
GO TO 10
9 TEMP=G(N,M)*CP(M)
BP=BP-(G(N,M)*SP(M))*FM(M)*PAR
10 BT=BT+TEMP*DP(N,M)*AR
8 BR=BR-TEMP*FN(N)*PAR
BP=BP/ST
B=SQRT(BT*BT+BP*BP+BR*BR)
RETURN
END

```

ORIGINAL PROGRAM
OF POOR QUALITY

